



Swansea University  
Prifysgol Abertawe



## Cronfa - Swansea University Open Access Repository

---

This is an author produced version of a paper published in:  
*International Journal for Numerical Methods in Engineering*

Cronfa URL for this paper:  
<http://cronfa.swan.ac.uk/Record/cronfa38853>

---

### **Paper:**

Li, Z., Cen, S., Wu, C., Shang, Y. & Li, C. (2018). High-performance geometric nonlinear analysis with the unsymmetric 4-node, 8-DOF plane element US-ATFQ4. *International Journal for Numerical Methods in Engineering*  
<http://dx.doi.org/10.1002/nme.5771>

---

This item is brought to you by Swansea University. Any person downloading material is agreeing to abide by the terms of the repository licence. Copies of full text items may be used or reproduced in any format or medium, without prior permission for personal research or study, educational or non-commercial purposes only. The copyright for any work remains with the original author unless otherwise specified. The full-text must not be sold in any format or medium without the formal permission of the copyright holder.

Permission for multiple reproductions should be obtained from the original author.

Authors are personally responsible for adhering to copyright and publisher restrictions when uploading content to the repository.

<http://www.swansea.ac.uk/library/researchsupport/ris-support/>

# High-performance geometric nonlinear analysis with the unsymmetric 4-node, 8-DOF plane element US-ATFQ4

Zhi Li <sup>1</sup>, Song Cen<sup>1,2,\*</sup>,†, Cheng-Jin Wu <sup>1</sup>, Yan Shang <sup>3</sup>, Chen-Feng Li <sup>4</sup>,

<sup>1</sup> *Department of Engineering Mechanics, School of Aerospace Engineering, Tsinghua University, Beijing 100084, China*

<sup>2</sup> *Key Laboratory of Applied Mechanics, School of Aerospace Engineering, Tsinghua University, Beijing 100084, China*

<sup>3</sup> *State Key Laboratory of Mechanics and Control of Mechanical Structures, College of Aerospace Engineering, Nanjing University of Aeronautics and Astronautics, Nanjing 210016, China*

<sup>4</sup> *College of Engineering, Swansea University, Swansea SA2 8PP, UK*

## SUMMARY

A recent unsymmetric 4-node, 8-DOF plane element US-ATFQ4, which exhibits excellent precision and distortion-resistance for linear elastic problems, is extended to geometric nonlinear analysis. Since the original linear element US-ATFQ4 contains the analytical solutions for plane pure bending, how to modify such formulae into incremental forms for nonlinear applications and design an appropriate updated algorithm become the key of the whole job. First, the analytical trial functions should be updated at each iterative step in the framework of updated Lagrangian (UL) formulation that takes the configuration at the beginning of an incremental step as the reference configuration during that step. Second, an appropriate stress update algorithm in which the Cauchy stresses are updated by the Hughes-Winget method is adopted to estimate current stress fields. Numerical examples show that the new nonlinear element US-ATFQ4 also possesses amazing performance for geometric nonlinear analysis, no matter regular or distorted meshes are used. It again demonstrates the advantages of the unsymmetric finite element method with analytical trial functions.

**KEY WORDS:** finite element; unsymmetric 4-node plane element; geometric nonlinear analysis; UL formulation; analytical trial function; mesh distortion

## 1. INTRODUCTION

---

\*Correspondence to: Song Cen, Department of Engineering Mechanics, School of Aerospace, Tsinghua University, Beijing 100084, China.  
†E-mail: censon@tsinghua.edu.cn

The traditional 4-node, 8-DOF isoparametric element with full integration scheme, denoted by Q4, is one of the most popular models adopted for two-dimensional (2D) finite element analysis. However, in many high-order problems, this model exhibits an over-stiff behavior and suffers from various locking problems, and this situation will become worse if distorted meshes are used [1, 2]. In order to improve the performance of element Q4, some researchers developed incompatible models, such as the element Q6 proposed by Wilson et al. [3] and its modified version QM6 proposed by Taylor et al. [4], the Abaqus incompatible elements CPS4I/CPE4I [5] with assumed strains [6], and so on. Although these incompatible models have reliable performance for regular meshes generally, they are still sensitive to mesh distortion and will lose most precision in distorted meshes. Reduced integration scheme was also suggested to resist over-stiff and sensitive problems to mesh distortion. Nevertheless, it may deteriorate the precision for stresses and bring *hourglass* problem (over-soft) [5]. During the past decades, numerous efforts have been made to look for robust 4-node, 8-DOF quadrilateral element models. In addition to the above incompatible and reduced integration schemes, some other techniques, including the hybrid stress method [7-12], the quasi-conforming method [13], the generalized conforming method [2], the improved enhanced strain method [14-16], the B-bar method [17], the quadrilateral area coordinate method [18-27], etc., can be found in related references. Although these models can improve the performance more or less, the sensitivity problem to mesh distortion has never been overcome from the outset. Specially, no element can overcome the obstacle stipulated by MacNeal's theorem [28, 29]: any 4-node, 8-DOF plane membrane element will either lock in in-plane bending or fail to pass a  $C_0$  patch test when the element's shape is an isosceles trapezoid, which means such elements must be sensitive to mesh distortions.

Recently, Cen *et al.* [30] developed an unsymmetric 4-node, 8-DOF plane element US-ATFQ4 based on the virtual work principle [31]. In the formulations of element US-ATFQ4, two different sets of shape functions are simultaneously used. The first set which comes from the traditional 4-node bilinear isoparametric element Q4 is employed as test functions, while the second set, which is employed as trial functions, uses analytical solutions for plane pure bending in terms of the second form of quadrilateral area coordinates (QACM-II) ( $S, T$ ) [24]. This element exhibits excellent

performance in rigorous tests and successfully breaks through the limitation defined by MacNeal's theorem [28, 29], that is to say, it is insensitive to various serious mesh distortions.

Actually, since mesh distortions will appear more easily due to large strains, or large displacements, or large rotations, a distortion-resistance finite element model should be more valuable in nonlinear analysis. For geometric nonlinear problems, there are usually three Lagrangian kinematic descriptions for finite element analysis [32], including total Lagrangian (TL) formulation, updated Lagrangian (UL) formulation and corotational (CR) formulation. The TL formulation requires that all quantities are referred to the original, undeformed configuration, while the UL formulation takes the current configuration, i.e. the configuration at the beginning of an incremental step, as the reference configuration during that step. In the CR formulation, the displacements and rotations are allowed to be arbitrarily large, but strains are limited to be small. Among these three formulations, the UL formulation is often preferred because it possesses better flexibility for solving various complicated nonlinear problems. Usually, it adopts the concept of Cauchy (physical) stress, and uses the rate-of-deformation as a measure of strain rate, but other measures of strain or strain rate can also be used [33]. Furthermore, a procedure for evaluating current stresses is required in the implementation of the UL formulation, and a so-called incrementally objective stress update scheme that can exactly account for the proper rotation of the stresses in a rigid body rotation for large deformation problems is needed. Hughes and Winget [34] introduced the concept of incremental objectivity, and Rashid [35] further distinguished it into weak objectivity and strong objectivity. Subsequently, Simo and Hughes [36] gave an extensive discussion on the incrementally objective stress update algorithms based on the concept of Lie derivatives.

Recently, new displacement-based 4-node, 8-DOF plane quadrilateral finite element models for analysis of geometric nonlinear problems can still be found in various literatures, such as the nonlinear quadrilateral area coordinate element AGQ6-I [23], the nonlinear quasi-conforming element [37], the nonlinear assumed strain MITC element [38], and so on. However, as previously mentioned, no model can break MacNeal's theorem, so that their performances cannot be guaranteed when severely distorted mesh appears. Some researchers hoped to solve this difficulty by introducing other new techniques, such as the 4-node Hu–Washizu elements based on skew coordinates

presented by Wisniewski *et al.* [39,40], the elements with the additional rotational degrees of freedom presented by Zouari *et al.* [41], the hybrid discontinuous Galerkin method proposed by Wulfinghoff *et al.* [42], the partition of unity-based ‘FE-meshfree’ method proposed by Rajendran *et al.* [43], and so on. Nevertheless, the computation costs also increase at the same time.

It is very interesting that whether the unsymmetric element US-ATFQ4 [30], which possesses high distortion-resistance for linear elastic problems, can be extended to nonlinear applications. However, some researchers negative this extension, they think that the approach, which employs the analytical solutions satisfying all governing equations for linear elasticity, restricts the element to linear elastic analysis [44]. In fact, the analytical trial functions are only the functions of physical coordinates with material constants. These coordinates and material constants can be updated referred to the current configuration at each iterative step, so that it is possible to use them as part of the incremental equations of the UL formulation.

The main purpose of this paper is to extend the 4-node, 8-DOF unsymmetric element US-ATFQ4 to the geometric nonlinear analysis. Since the original linear element US-ATFQ4 contains the analytical solutions for plane pure bending, how to modify such formulae into incremental forms for nonlinear applications and design an appropriate updated algorithm become the key of the whole job. As many engineering materials still present small strain state in practice [45], this paper will only focus on small strain with large displacement/rotation problems. The content of the work is organized as follows: In Section 2, the UL formulation is briefly reviewed. In Section 3, the formulations of element US-ATFQ4 for geometric nonlinear analysis are established, and the numerical implementation in Abaqus UEL [5] is also introduced. In the following Section 4, several typical geometric nonlinear numerical examples are employed to test the performance of the present formulations. It can be seen that the proposed nonlinear element US-ATFQ4 can provide excellent results in both regular and distorted meshes, which demonstrates the advantages of the new unsymmetric finite element method with linear analytical trial functions.

## 2. BRIEF REVIEW ON THE UPDATED LAGRANGIAN FORMULATION

As shown in Figure 1, a general deformable body experiencing large displacement motion in the

Cartesian coordinate system is considered.  $C_0$ ,  $C_1$  and  $C_2$  are the configurations of the body at times 0,  $t$  and  $t+\Delta t$ , respectively. The Cartesian coordinates of a point P within the body at these three different configurations are  $({}^0x, {}^0y, {}^0z)$ ,  $({}^tx, {}^ty, {}^tz)$  and  $({}^{t+\Delta t}x, {}^{t+\Delta t}y, {}^{t+\Delta t}z)$ , respectively, in which the left superscripts refer to the times for three different configurations of the body. So the displacement increments are given by  $u_i = {}^{t+\Delta t}x_i - {}^tx_i, (i=1,2,3)$ . Note: two types of notation, indicial notation and matrix notation, are both used in this paper. In order to avoid confusion with nodal values, the Cartesian coordinates are expressed by  $(x, y, z)$ , rather than the form with subscripts, i.e.  $x_1 = x, x_2 = y, x_3 = z$ . For the components of a vector, their subscripts are also expressed by  $(x, y, z)$ , rather than  $(1, 2, 3)$ , for example, the components of the displacement increments  $u_i$  in three dimensions are  $u_1 = u_x, u_2 = u_y, u_3 = u_z$ . The nodal indices are indicated by upper case letters, for example,  $u_{iI}$  is the  $i$ -component of the displacement increments at node  $I$  [33]. In conformance with the rules of Einstein notation, indices repeated twice in a term should be summed.

In the updated Lagrangian (UL) formulation, the equilibrium equation of the body at time  $t+\Delta t$  referred to configuration  $C_1$  can be derived by the principle of virtual displacements, and expressed by [46]:

$$\int_{tV} {}^{t+\Delta t}S_{ij} \delta {}^{t+\Delta t}\varepsilon_{ij} d^tV - \left( \int_{tV} {}^{t+\Delta t}f_i \delta u_i d^tV + \int_{tS} {}^{t+\Delta t}t_i \delta u_i d^tS \right) = 0, \quad (1)$$

where  ${}^{t+\Delta t}S_{ij}$  and  ${}^{t+\Delta t}\varepsilon_{ij}$  denote, respectively, the second Piola-Kirchoff stress tensor and the Green-Lagrange strain tensor, which are defined at time  $t+\Delta t$  and referred to configuration  $C_1$ ; and

$$\int_{tV} {}^{t+\Delta t}f_i \delta u_i d^tV + \int_{tS} {}^{t+\Delta t}t_i \delta u_i d^tS = \delta {}^{t+\Delta t}W_{ext}, \quad (2)$$

where  $\delta {}^{t+\Delta t}W_{ext}$  denotes the external virtual work at time  $t+\Delta t$ ;  ${}^{t+\Delta t}f_i$  and  ${}^{t+\Delta t}t_i$  denote, respectively, the components of the body force vector and the boundary traction vector applied to configuration  $C_2$  and referred to configuration  $C_1$ ;  $\delta u_i$  denotes virtual displacement vector imposed on configuration  $C_2$ ;  ${}^tV$  and  ${}^tS$  denote the volume and the surface area of the body under discussion referred to configuration  $C_1$ , respectively.

Equation (1) is a nonlinear equation for solving the displacement increments  $u_i$ . In order to make it computationally tractable, equation (1) is usually linearized by introducing following relations and approximations [46]:

$${}^{t+\Delta t}{}_t\mathbf{S}_{ij} = {}^t\sigma_{ij} + {}_t\mathbf{S}_{ij}, ({}^t\mathbf{S}_{ij} \equiv {}^t\sigma_{ij}), \quad (3)$$

$$\begin{cases} {}^{t+\Delta t}{}_t\boldsymbol{\varepsilon}_{ij} = {}_t\boldsymbol{\varepsilon}_{ij} = {}_t\mathbf{e}_{ij} + {}_t\boldsymbol{\eta}_{ij} \\ {}_t\mathbf{e}_{ij} = \frac{1}{2}({}_t\mathbf{u}_{i,j} + {}_t\mathbf{u}_{j,i}); \quad {}_t\boldsymbol{\eta}_{ij} = \frac{1}{2}{}_t\mathbf{u}_{k,i}{}_t\mathbf{u}_{k,j} \end{cases}, \quad (4)$$

$${}_t\mathbf{S}_{ij} = {}_t\mathbf{C}_{ijrs}{}_te_{rs}; \quad \delta{}_t\boldsymbol{\varepsilon}_{ij} = \delta{}_te_{ij}, \quad (5)$$

where  ${}^t\sigma_{ij}$  are the components of the known Cauchy stresses at time  $t$ ;  ${}_te_{ij}$  and  ${}_t\boldsymbol{\eta}_{ij}$  are the linear and nonlinear incremental strains referred to configuration  $C_1$ , respectively;  ${}_tu_{i,j} = \frac{\partial u_i}{\partial x_j}$  are the derivatives of the displacement increments  $u_i$  refer to the coordinates  ${}^tx_j$ ;  ${}_t\mathbf{C}_{ijrs}$  are the components of the incremental stress-strain relation tensor at time  $t$  referred to configuration  $C_1$ .

Substitution of equations (3), (4) and (5) into equation (1) yields the linearized equilibrium equation:

$$\int_{tV} {}_t\mathbf{C}_{ijrs}{}_te_{rs}\delta{}_te_{ij}d^tV + \int_{tV} {}^t\sigma_{ij}\delta{}_t\boldsymbol{\eta}_{ij}d^tV = \delta{}^{t+\Delta t}\mathbf{W}_{ext} - \int_{tV} {}^t\sigma_{ij}\delta{}_te_{ij}d^tV. \quad (6)$$

### 3. EXTENSION OF THE UNSYMMETRIC 4-NODE, 8-DOF PLANE ELEMENT US-ATFQ4 FOR GEOMETRIC NONLINEAR ANALYSIS

#### 3.1 Geometric nonlinear Formulations for element US-ATFQ4

In this section, the unsymmetric 4-node plane membrane element US-ATFQ4 [30], which can perfectly break through MacNeal's theorem [28, 29] and possesses excellent distortion-resistance for linear elasticity [30], is extended to applications for geometric nonlinear problems.

A 4-node, 8-DOF plane quadrilateral element is shown in Figure 2. Nodes 1, 2, 3 and 4 are the corner nodes;  $({}^tx_I, {}^ty_I)$ ,  $({}^tS_I, {}^tT_I)$  are, respectively, the Cartesian coordinates and quadrilateral area coordinates (QACM-II) [24] (see Appendix A) of the corner node  $I$  ( $I = 1, 2, 3, 4$ ) at time  $t$ ;  $u_{\alpha I}$  is

the  $\alpha$ -component ( $\alpha=1,2$ ) of the displacement increments at node  $I$ . For the unsymmetric element US-ATFQ4 [30], two different sets of interpolation functions for displacement fields are simultaneously used. The first set is for the virtual displacement fields  $\{\delta\mathbf{u}\}$  and employs the shape functions of the traditional 4-node bilinear isoparametric element:

$$\{\delta\mathbf{u}\} = \begin{Bmatrix} \delta u_x \\ \delta u_y \end{Bmatrix} = [\bar{\mathbf{N}}] \{\delta\Delta\mathbf{q}^e\}, \quad (7)$$

where

$$\{\delta\Delta\mathbf{q}^e\} = [\delta u_{x1} \quad \delta u_{y1} \quad \delta u_{x2} \quad \delta u_{y2} \quad \delta u_{x3} \quad \delta u_{y3} \quad \delta u_{x4} \quad \delta u_{y4}]^T, \quad (8)$$

$$[\bar{\mathbf{N}}] = \begin{bmatrix} \bar{N}_1 & 0 & \bar{N}_2 & 0 & \bar{N}_3 & 0 & \bar{N}_4 & 0 \\ 0 & \bar{N}_1 & 0 & \bar{N}_2 & 0 & \bar{N}_3 & 0 & \bar{N}_4 \end{bmatrix}, \quad (9)$$

with

$$\bar{N}_I = \frac{1}{4}(1 + \xi_I \xi)(1 + \eta_I \eta), \quad (I=1,2,3,4). \quad (10)$$

And  $\{\delta\Delta\mathbf{q}^e\}$  is the nodal virtual displacement vector;  $[\bar{\mathbf{N}}]$  is the interpolation function matrix of traditional 4-node bilinear isoparametric element;  $(\xi_I, \eta_I)$  are the nodal isoparametric coordinates.

The second set is for the *real* incremental displacement fields  $\{\mathbf{u}\}$  and adopts a composite coordinate interpolation scheme with analytical trial functions:

$$\{\mathbf{u}\} = \begin{Bmatrix} u_x \\ u_y \end{Bmatrix} = [\mathbf{P}] \{\boldsymbol{\alpha}\} = \begin{bmatrix} 1 & 0 & {}^t x & 0 & {}^t y & 0 & {}^t U_7 & {}^t U_8 \\ 0 & 1 & 0 & {}^t x & 0 & {}^t y & {}^t V_7 & {}^t V_8 \end{bmatrix} \begin{Bmatrix} \alpha_1 \\ \alpha_2 \\ \alpha_3 \\ \mathbf{M} \\ \alpha_8 \end{Bmatrix} \quad (11)$$

where  $\alpha_i$  ( $i=1\sim 8$ ) are eight undetermined coefficients;  ${}^t U_7, {}^t V_7, {}^t U_8$  and  ${}^t V_8$  are the linear displacement solutions for plane pure bending in arbitrary direction and in terms of the second form of quadrilateral area coordinates (QACM-II) ( $S, T$ ) [24] (see Appendix A) at time  $t$ . The detailed expressions of  ${}^t U_7, {}^t V_7, {}^t U_8$  and  ${}^t V_8$  are derived by reference [30] and given in Appendix B. Substitution of nodal coordinates (including Cartesian and QACM-II) and nodal displacement

increments into equation (11) yields:

$$\{\mathbf{u}\} = \begin{Bmatrix} u_x \\ u_y \end{Bmatrix} = [{}^t\hat{\mathbf{N}}] \{\Delta\mathbf{q}^e\}, \quad (12)$$

where

$$\{\Delta\mathbf{q}^e\} = [u_{x1} \quad u_{y1} \quad u_{x2} \quad u_{y2} \quad u_{x3} \quad u_{y3} \quad u_{x4} \quad u_{y4}]^T, \quad (13)$$

$$[{}^t\hat{\mathbf{N}}] = \begin{bmatrix} {}^t\hat{N}_{11} & {}^t\hat{N}_{12} & {}^t\hat{N}_{13} & {}^t\hat{N}_{14} & {}^t\hat{N}_{15} & {}^t\hat{N}_{16} & {}^t\hat{N}_{17} & {}^t\hat{N}_{18} \\ {}^t\hat{N}_{21} & {}^t\hat{N}_{22} & {}^t\hat{N}_{23} & {}^t\hat{N}_{24} & {}^t\hat{N}_{25} & {}^t\hat{N}_{26} & {}^t\hat{N}_{27} & {}^t\hat{N}_{28} \end{bmatrix}. \quad (14)$$

And  $\{\Delta\mathbf{q}^e\}$  is the nodal displacement increment vector;  $[{}^t\hat{\mathbf{N}}]$  is the composite coordinate interpolation functions matrix. The detailed expressions of  $[{}^t\hat{\mathbf{N}}]$  are given in Appendix B. It can be seen that the interpolation functions matrix  $[{}^t\hat{\mathbf{N}}]$  depends on current coordinates, so the analytical trial functions should be updated at each iterative step in the framework of updated Lagrangian formulation.

The first term at the left side of equation (6) can be rewritten as following matrix form:

$$\begin{aligned} & \int_{tV} {}^tC_{ijrs} {}^te_{rs} \delta {}^te_{ij} d^tV \\ &= \sum_e \int_{tV_e} \begin{Bmatrix} \delta {}^tu_{x,x} \\ \delta {}^tu_{y,y} \\ \delta {}^tu_{x,y} + \delta {}^tu_{y,x} \end{Bmatrix}^T \begin{bmatrix} {}^tC_{11} & {}^tC_{12} & {}^tC_{16} \\ {}^tC_{21} & {}^tC_{22} & {}^tC_{26} \\ {}^tC_{61} & {}^tC_{62} & {}^tC_{66} \end{bmatrix} \begin{Bmatrix} {}^tu_{x,x} \\ {}^tu_{y,y} \\ {}^tu_{x,y} + {}^tu_{y,x} \end{Bmatrix} d^tV, \quad (15) \\ &= \sum_e \int_{tV_e} \{\delta\Delta\mathbf{q}^e\}^T [{}^t\bar{\mathbf{B}}_L]^T [{}^t\mathbf{C}] [{}^t\hat{\mathbf{B}}_L] \{\Delta\mathbf{q}^e\} d^tV \end{aligned}$$

where

$$[{}^t\bar{\mathbf{B}}_L] = \begin{bmatrix} {}^t\bar{N}_{1,x} & 0 & \dots & {}^t\bar{N}_{4,x} & 0 \\ 0 & {}^t\bar{N}_{1,y} & \dots & 0 & {}^t\bar{N}_{4,y} \\ {}^t\bar{N}_{1,y} & {}^t\bar{N}_{1,x} & \dots & {}^t\bar{N}_{4,y} & {}^t\bar{N}_{4,x} \end{bmatrix}, \quad (16)$$

$$[{}^t\hat{\mathbf{B}}_L] = \begin{bmatrix} {}^t\hat{N}_{11,x} & {}^t\hat{N}_{12,x} & \dots & {}^t\hat{N}_{17,x} & {}^t\hat{N}_{18,x} \\ {}^t\hat{N}_{21,y} & {}^t\hat{N}_{22,y} & \dots & {}^t\hat{N}_{27,y} & {}^t\hat{N}_{28,y} \\ {}^t\hat{N}_{11,y} + {}^t\hat{N}_{21,x} & {}^t\hat{N}_{12,y} + {}^t\hat{N}_{22,x} & \dots & {}^t\hat{N}_{17,y} + {}^t\hat{N}_{27,x} & {}^t\hat{N}_{18,y} + {}^t\hat{N}_{28,x} \end{bmatrix} \{\mathbf{u}\}. \quad (17)$$

The second term at the left side of equation (6) can be rewritten as

$$\begin{aligned}
& \int_{tV} {}^t\sigma_{ij}\delta_t\eta_{ij}d^tV \\
&= \sum_e \int_{tV_e} \left[ {}^t\sigma_{xx}(\delta u_{x,x}u_{x,x} + \delta u_{y,x}u_{y,x}) + {}^t\sigma_{yy}(\delta u_{x,y}u_{x,y} + \delta u_{y,y}u_{y,y}) \right. \\
&\quad \left. + {}^t\sigma_{xy}(\delta u_{x,x}u_{x,y} + \delta u_{y,x}u_{y,y} + \delta u_{x,y}u_{x,x} + \delta u_{y,y}u_{y,x}) \right] d^tV, \quad (18) \\
&= \sum_e \int_{tV_e} \begin{Bmatrix} \delta u_{x,x} \\ \delta u_{x,y} \\ \delta u_{y,x} \\ \delta u_{y,y} \end{Bmatrix}^T \begin{bmatrix} {}^t\sigma_{xx} & {}^t\sigma_{xy} & 0 & 0 \\ {}^t\sigma_{yx} & {}^t\sigma_{yy} & 0 & 0 \\ 0 & 0 & {}^t\sigma_{xx} & {}^t\sigma_{xy} \\ 0 & 0 & {}^t\sigma_{yx} & {}^t\sigma_{yy} \end{bmatrix} \begin{Bmatrix} u_{x,x} \\ u_{x,y} \\ u_{y,x} \\ u_{y,y} \end{Bmatrix} d^tV \\
&= \sum_e \int_{tV_e} \{\delta\Delta\mathbf{q}^e\}^T [{}^t\bar{\mathbf{B}}_{NL}]^T [{}^t\boldsymbol{\sigma}] [{}^t\hat{\mathbf{B}}_{NL}] \{\Delta\mathbf{q}^e\} d^tV
\end{aligned}$$

where

$$[{}^t\bar{\mathbf{B}}_{NL}] = \begin{bmatrix} {}^t\bar{N}_{1,x} & 0 & \dots & {}^t\bar{N}_{4,x} & 0 \\ {}^t\bar{N}_{1,y} & 0 & \dots & {}^t\bar{N}_{4,y} & 0 \\ 0 & {}^t\bar{N}_{1,x} & \dots & 0 & {}^t\bar{N}_{4,x} \\ 0 & {}^t\bar{N}_{1,y} & \dots & 0 & {}^t\bar{N}_{4,y} \end{bmatrix}, \quad (19)$$

$$[{}^t\hat{\mathbf{B}}_{NL}] = \begin{bmatrix} {}^t\hat{N}_{11,x} & {}^t\hat{N}_{12,x} & \dots & {}^t\hat{N}_{17,x} & {}^t\hat{N}_{18,x} \\ {}^t\hat{N}_{11,y} & {}^t\hat{N}_{12,y} & \dots & {}^t\hat{N}_{17,y} & {}^t\hat{N}_{18,y} \\ {}^t\hat{N}_{21,x} & {}^t\hat{N}_{22,x} & \dots & {}^t\hat{N}_{27,x} & {}^t\hat{N}_{28,x} \\ {}^t\hat{N}_{21,y} & {}^t\hat{N}_{22,y} & \dots & {}^t\hat{N}_{27,y} & {}^t\hat{N}_{28,y} \end{bmatrix}. \quad (20)$$

The last term at the right side of equation (6) can be rewritten as

$$\begin{aligned}
\int_{tV} {}^t\sigma_{ij}\delta_t e_{ij}d^tV &= \sum_e \int_{tV_e} \begin{Bmatrix} \delta_t e_{xx} \\ \delta_t e_{yy} \\ 2\delta_t e_{xy} \end{Bmatrix}^T \begin{Bmatrix} {}^t\sigma_{xx} \\ {}^t\sigma_{yy} \\ {}^t\sigma_{xy} \end{Bmatrix} d^tV \\
&= \sum_e \int_{tV_e} \{\delta_t \mathbf{e}\}^T \{\boldsymbol{\sigma}\} d^tV = \sum_e \int_{tV_e} \{\delta\Delta\mathbf{q}^e\}^T [{}^t\bar{\mathbf{B}}_L]^T \{\boldsymbol{\sigma}\} d^tV
\end{aligned} \quad (21)$$

Thus, from equations (15-21), equation (6) can be expressed by following matrix form

$$\begin{aligned}
& \sum_e \int_{tV_e} \{\delta\Delta\mathbf{q}^e\}^T [{}^t\bar{\mathbf{B}}_L]^T [{}^t\mathbf{C}] [{}^t\hat{\mathbf{B}}_L] \{\Delta\mathbf{q}^e\} d^tV + \sum_e \int_{tV_e} \{\delta\Delta\mathbf{q}^e\}^T [{}^t\bar{\mathbf{B}}_{NL}]^T [{}^t\boldsymbol{\sigma}] [{}^t\hat{\mathbf{B}}_{NL}] \{\Delta\mathbf{q}^e\} d^tV \\
&= \sum_e \{\delta\Delta\mathbf{q}^e\}^T \{{}^{t+\Delta t}\mathbf{F}_{ext}^e\} - \sum_e \int_{tV_e} \{\delta\Delta\mathbf{q}^e\}^T [{}^t\bar{\mathbf{B}}_L]^T \{\boldsymbol{\sigma}\} d^tV
\end{aligned} \quad (22)$$

Since  $\{\delta\Delta\mathbf{q}^e\}$  in above equation are arbitrary, the following finite element equations can be obtained:

$$\sum_e \left[ {}^t \mathbf{K}_T^e \right] \{ \Delta \mathbf{q}^e \} = \sum_e \left\{ {}^{t+\Delta t} {}^t \mathbf{R}^e \right\}, \quad (23)$$

where

$$\left[ {}^t \mathbf{K}_T^e \right] = \left[ {}^t \mathbf{K}_L^e \right] + \left[ {}^t \mathbf{K}_{NL}^e \right], \quad (24)$$

$$\left\{ {}^{t+\Delta t} {}^t \mathbf{R}^e \right\} = \left\{ {}^{t+\Delta t} {}^t \mathbf{F}_{ext}^e \right\} - \left\{ {}^t \mathbf{F}_{int}^e \right\}, \quad (25)$$

$$\left[ {}^t \mathbf{K}_L^e \right] = \int_{V_e} \left[ {}^t \bar{\mathbf{B}}_L \right]^T \left[ {}^t \mathbf{C} \right] \left[ {}^t \hat{\mathbf{B}}_L \right] d^t V, \quad (26)$$

$$\left[ {}^t \mathbf{K}_{NL}^e \right] = \int_{V_e} \left[ {}^t \bar{\mathbf{B}}_{NL} \right]^T \left[ {}^t \hat{\boldsymbol{\sigma}} \right] \left[ {}^t \hat{\mathbf{B}}_{NL} \right] d^t V, \quad (27)$$

$$\left\{ {}^{t+\Delta t} {}^t \mathbf{F}_{ext}^e \right\} = \int_{V_e} \left[ \bar{\mathbf{N}} \right]^T \left\{ {}^{t+\Delta t} {}^t \mathbf{f} \right\} d^t V + \int_{S_e} \left[ \bar{\mathbf{N}} \right]^T \left\{ {}^{t+\Delta t} {}^t \mathbf{t} \right\} d^t S, \quad (28)$$

$$\left\{ {}^t \mathbf{F}_{int}^e \right\} = \int_{V_e} \left[ {}^t \bar{\mathbf{B}}_L \right]^T \left\{ {}^t \boldsymbol{\sigma} \right\} d^t V. \quad (29)$$

The increments of the nodal displacements from the time  $t$  to  $t+\Delta t$ ,  $\{ \Delta \mathbf{q}^e \}$ , can be obtained by solving equation (23). Usually,  $\{ \Delta \mathbf{q}^e \}$  will be used to update the displacements, strains, and stresses at time  $t+\Delta t$ . Here, in order to obtain the values of Cauchy stress efficiently and accurately, instead of usual strategy, and the Hughes-Winget method [34] is adopted to update the stresses at time  $t + \Delta t$  :

$$\left[ {}^{t+\Delta t} \boldsymbol{\sigma} \right] = \left[ \Delta \mathbf{R} \right] \left[ {}^t \boldsymbol{\sigma} \right] \left[ \Delta \mathbf{R} \right]^T + \left[ \Delta \boldsymbol{\sigma} \right], \quad (30)$$

where

$$\left[ {}^{t+\Delta t} \boldsymbol{\sigma} \right] = \begin{bmatrix} {}^{t+\Delta t} \sigma_{xx} & {}^{t+\Delta t} \sigma_{xy} \\ {}^{t+\Delta t} \sigma_{yx} & {}^{t+\Delta t} \sigma_{yy} \end{bmatrix}; \quad \left[ \Delta \boldsymbol{\sigma} \right] = \begin{bmatrix} \Delta \sigma_{xx} & \Delta \sigma_{xy} \\ \Delta \sigma_{yx} & \Delta \sigma_{yy} \end{bmatrix}, \quad (31)$$

$$\left[ \Delta \mathbf{R} \right] = \begin{bmatrix} \Delta R_{xx} & \Delta R_{xy} \\ \Delta R_{yx} & \Delta R_{yy} \end{bmatrix} = \left[ \mathbf{I} - \frac{1}{2} \Delta \mathbf{W} \right]^{-1} \left[ \mathbf{I} + \frac{1}{2} \Delta \mathbf{W} \right], \quad \left[ \mathbf{I} \right] = \begin{bmatrix} 1 & 0 \\ 0 & 1 \end{bmatrix}, \quad (32)$$

$$\left[ \Delta \mathbf{W} \right] = \begin{bmatrix} \Delta W_{xx} & \Delta W_{xy} \\ \Delta W_{yx} & \Delta W_{yy} \end{bmatrix}$$

with

$$\Delta W_{\alpha\beta} = \frac{1}{2} \left( {}^{t+\Delta t/2} u_{\alpha,\beta} - {}^{t+\Delta t/2} u_{\beta,\alpha} \right), \quad (33)$$

$${}^{t+\Delta t/2} u_{\alpha,\beta} = \frac{\partial u_\alpha}{\partial {}^{t+\Delta t/2} x_\beta}; \quad {}^{t+\Delta t/2} x_\beta = \frac{1}{2} \left( {}^t x_\beta + {}^{t+\Delta t} x_\beta \right), \quad (\alpha, \beta = 1, 2). \quad (34)$$

$\Delta W_{\alpha\beta}$ , which are defined at the midpoint of the time interval, are the increments in spin;  $\Delta R_{\alpha\beta}$  are the increments in rotation; and the subscripts  $t$  and  $t+\Delta t$ , respectively, refer to the beginning and the end of the increment.

For the isotropic elastic case, we have:

$$\begin{Bmatrix} \Delta\sigma_{xx} \\ \Delta\sigma_{yy} \\ \Delta\sigma_{xy} \end{Bmatrix} = \frac{E'}{1-\mu'^2} \begin{bmatrix} 1 & \mu' & 0 \\ \mu' & 1 & 0 \\ 0 & 0 & \frac{1-\mu'}{2} \end{bmatrix} \begin{Bmatrix} \Delta D_{xx} \\ \Delta D_{yy} \\ 2\Delta D_{xy} \end{Bmatrix}, \quad (35)$$

where  $E' = E$  and  $\mu' = \mu$  for plane stress problem, whereas  $E' = E/(1-\mu^2)$  and  $\mu' = \mu/(1-\mu)$  for plane strain problem, in which  $E$  and  $\mu$  are Young's modulus and Poisson's ratio, respectively; and  $\Delta D_{\alpha\beta}$ , which are also defined at the midpoint of the time interval, are the strain increments,

$$\Delta D_{\alpha\beta} = \frac{1}{2} \left( {}_{t+\Delta t/2}u_{\alpha,\beta} + {}_{t+\Delta t/2}u_{\beta,\alpha} \right), \quad (\alpha, \beta = 1, 2). \quad (36)$$

### 3.2 Numerical implementation

In this paper, the present geometric nonlinear formulations of element US-ATFQ4 will be compiled and implemented in commercial software SIMULA Abaqus via the user element subroutine (UEL) [5], and the corresponding flowchart is given by Figure 3. First, an input-file is written with Abaqus keywords [5] to define an analysis. Then, this input-file is submitted to Abaqus/Standard and the program is run to solve specified problems. All results will be output by automatically writing in an *Odb* file. Figure 3 also shows the incremental-iterative Newton-Raphson schemes for solving the nonlinear problems.

All terms of the element formulations are evaluated by using a  $2 \times 2$  Gauss integration scheme. Figure 4 plots the computation flowchart of the nonlinear formulations of element US-ATFQ4 in UEL.

## 4. NUMERICAL EXAMPLES

In this section, four examples using traditional regular and new distorted mesh divisions are adopted to assess the performance of the new formulations. All nonlinear finite element equations are solved by

the full Newton-Raphson method and automatic incrementation control scheme (the size of time increments is automatically adjusted according to convergence) embedded in Abaqus [5]. The initial size of time increment is set to 0.1 (the total time is 1) because of the highly geometric nonlinearity. Results obtained by some other plane quadrilateral models, as listed below, are also given for comparison.

*Plane quadrilateral element models for geometrically nonlinear analysis:*

- CPS4/CPE4 (Q4): the 4-node isoparametric elements in Abaqus, with full  $2 \times 2$  integration scheme, and for plane stress and strain states, respectively [5].
- CPS4R/CPE4R: the 4-node isoparametric elements in Abaqus, with reduced  $1 \times 1$  integration scheme and enhanced hourglass control approach, for plane stress and strain states, respectively [5].
- CPS4I/CPE4I: the 4-node nonconforming isoparametric elements in Abaqus, with enhanced assumed strain, and for plane stress and strain states, respectively [5].
- CPS8/CPE8: the 8-node isoparametric elements in Abaqus, with full  $3 \times 3$  integration scheme, and for plane stress and strain states, respectively [5].
- HW14-S: the mixed 4-node Hu–Washizu element based on skew coordinates proposed by Wisniewski *et al.* [39].
- HW18-SS: the mixed/enhanced 4-node Hu–Washizu element based on skew coordinates proposed by Wisniewski *et al.* [39].
- PFR4: the 4-node plane quadrilateral element with rotational degrees of freedom proposed by Zouari *et al.* [41].
- PFR4I: the 4-node nonconforming plane quadrilateral element with rotational degrees of freedom proposed by Zouari *et al.* [41].
- QM6: the nonlinear 4-node nonconforming plane quadrilateral element proposed by Battini [47], which was extended from the linear element QM6 proposed by Taylor *et al.* [4].
- Qnew: the nonlinear 4-node plane quadrilateral element proposed by Battini [47], which was extended from the linear element proposed by Fredriksson *et al.* [48].

#### 4.1 Cantilever beam subjected to end shear force

As shown in Figure 5, a slender elastic cantilever beam is subjected to a resultant shear force  $P$  at its free end. The reference results of the tip vertical and horizontal displacements have been reported by Sze et al. in [49]. Two mesh cases,  $1 \times 10$  elements with regular rectangle and distorted (isosceles trapezoid) shapes, are considered. The material (Young's modulus  $E$  and Poisson's ratio  $\mu$ ) and the geometry parameters are also given in Figure 5.

Figure 6 plots the deformed shapes obtained by elements US-ATFQ4, CPE4, CPE4I, CPE4R and CPE8. And the resulting load-displacement curves of US-ATFQ4 compared with CPE4, CPE4I and CPE8 are given in Figure 7. Table I lists the total number of increments NINC and iterations NITER required for obtaining the converged ultimate solutions using two mesh cases. As described in the beginning of section 4, during the whole computation process, the time increment is automatically adjusted according to the convergence. Here, a fixed time increment case is also tested. Table II gives the results of the vertical and horizontal tip displacements obtained by a fixed time increment size 0.1 (i.e., NINC=10).

For the regular mesh (distortion parameter  $\delta=0$ ), it can be observed that the results of the present element US-ATFQ4 agree very well with the reference curves. Element US-ATFQ4 is found to be more accurate than the Abaqus nonconforming model CPE4I and CPE4R, while CPE4 shows a very poor precision. For distorted mesh ( $\delta=0.05$ ), the proposed element US-ATFQ4 still keeps high accuracy. However, element CPE4I and CPE4R only provide very poor results similar to those obtained by CPE4. Furthermore, although the degrees of freedom of element US-ATFQ4 are much fewer than those of 8-node element CPE8, the results obtained by US-ATFQ4 are found to be better than those given by CPE8 for both two mesh cases. From Table II, it can be seen that the proposed element US-ATFQ4 can also produce excellent results when the fixed time increment 0.1 is used.

Besides, this example is redone with a non-zero Poisson's ratio,  $\mu=0.3$ , under plane stress conditions. The reference results of the tip vertical and horizontal displacements are obtained by using CPS8 with a fine mesh ( $2 \times 200$  rectangular elements). The resulting load-displacement curves of US-ATFQ4 compared with CPS4, CPS4I and CPS8 are given in Figure 8. The same conclusions as discussed above can be drawn.

Another similar example proposed by Wisniewski *et al.* [39] is also taken into consideration. The

only differences come from material and geometry parameters:  $E=10^6$ ,  $\mu=0.3$ ,  $L=100$ ,  $b=1$ ,  $h=1$  and the resultant shear force  $P = 200$ . The final rotation of this cantilever's tip is close to  $90^\circ$ . The reference results of the tip vertical and horizontal displacements are also obtained by using CPS8 with a fine mesh ( $2 \times 200$  rectangular elements). The resulting load-displacement curves of US-ATFQ4 (with  $1 \times 20$  rectangular elements) compared with HW14-S and HW18-SS (both with  $1 \times 100$  rectangular elements) are given in Figure 9. It can be seen that the proposed element US-ATFQ4 can produce excellent results with coarse mesh.

#### 4.2 Cantilever beam subjected to end moment

As shown in Figure 10, a slender cantilever beam is subjected to a resultant moment  $M$  at its free end. All material and geometry parameters are also given in Figure 10. The analytical solution for this problem is  $R=EI/M$  [49], where  $I$  is the section moment of inertia, and  $R$  is the radius of a circular which the cantilever beam forms. Hence, when the end resultant moment  $M$  is taken to be  $2\pi EI/L$ , the cantilever beam will bend to be a circle. The analytical solutions of the end moment against tip deflections have been given in reference [49].

Two mesh cases,  $1 \times 10$  regular rectangle elements and  $1 \times 20$  distorted (isosceles trapezoid) elements, are considered. The deformed shapes obtained by US-ATFQ4, CPE4, CPE4I, CPE4R and CPE8 are plotted in Figure 11. In addition, the load-displacement curves of US-ATFQ4 compared with CPE4, CPE4I and CPE8 are shown in Figure 12. Table III lists the total number of increments NINC and iterations NITER required for obtaining the converged ultimate solutions. And Table IV lists the vertical and horizontal tip displacements obtained by a fixed time increment 0.01 (i.e. NINC=100).

For the regular mesh with  $1 \times 10$  rectangular elements ( $\delta=0$ ), elements CPE4, CPE4I, CPE4R and even CPE8 cannot provide good results. On the contrary, under the same mesh, the results obtained by the present element US-ATFQ4 exhibit high accuracy. For the mesh with  $1 \times 20$  distorted elements ( $\delta=0.03$ ), the results of CPE4I and CPE4R are much worse than those obtained by using the  $1 \times 10$  regular mesh. But it can be seen that the solutions of US-ATFQ4 can still keep high accuracy. Similar to the previous example, although the degrees of freedom of CPE8 are much more than those of US-ATFQ4, US-ATFQ4 still performs better than CPE8 under both regular and distorted meshes.

Besides, this example is redone with a non-zero Poisson's ratio,  $\mu=0.3$ , under plane stress

conditions. The reference results of the tip vertical and horizontal displacements are obtained by using CPS8 with a fine mesh ( $2 \times 200$  rectangular elements). The resulting load-displacement curves of US-ATFQ4 compared with CPS4, CPS4I and CPS8 are given in Figure 13. The same conclusions as discussed above can be drawn.

#### 4.3 Angle frame

As shown in Figure 14, an angle frame structure, which is assumed to be under plane stress state, is clamped at left end and subjected to a uniformly distributed horizontal force  $F$  at right end. The material and geometry parameters are also given in Figure 14. The reference results are obtained by using CPS8 with a fine mesh (304 rectangular elements). Two mesh cases, (i) regular mesh with seven rectangular elements suggested by Zouari et al. in [41] and (ii) distorted mesh with nineteen distorted (isosceles trapezoid) elements suggested by Battini in [47], are considered. The deformed shape obtained by US-ATFQ4, CPS4, CPS4I compared with the reference deformed configuration are plotted in Figure 15. And the load-displacement curves of US-ATFQ4 compared with CPS4, CPS4I, PFR4 [41], PFR4I [41], QM6 [47] and Qnew [47] obtained by two meshes are shown in Figure 16. Table V lists the total number of increments NINC and iterations NITER required for obtaining the converged ultimate solutions.

For the regular mesh, elements US-ATFQ4, PFR4I and CPS4I all can agree well with the reference configuration obtained by CPS8 with fine mesh. And for the distorted mesh, US-ATFQ4 can still keep high accuracy, while CPS4I, QM6 and Qnew lose their precision greatly.

#### 4.4 Lee's frame buckling problem

The Lee's frame buckling problem is one of the NAFEMS (National Agency for Finite Element Methods and Standards) proposed benchmarks [50]. As shown in Figure 17, two mesh cases with twenty-five regular rectangle elements and twenty-five distorted (isosceles trapezoid) elements are considered. In order to study the post-buckling nonlinear behavior of the frame at point A, the modified Riks method [5, 45] is employed here. In such Riks method, the load magnitude is taken as an additional unknown, and the loads and the displacements are solved simultaneously. Unlike the normal incremental-iterative solution strategy under load control, the Riks method augments the

n-dimensional space of unknown displacements to an (n+1)-dimensional space of unknowns. So, another quantity, arc length  $l$ , must be used to measure the progress of solution along the static equilibrium path in load-displacement space, i.e. a path-following constraint should be added. More details about the Riks method were explained in [45].

Similar to previous examples, the automatic incrementation control scheme is chosen, and the initial increment size in arc length along the static equilibrium path  $\Delta l_{in}$ , the maximum arc length increment  $\Delta l_{max}$ , and the maximum value of the load proportionality factor  $\lambda_{end}$  are set to 0.1, 1, 30, respectively. The reference results are obtained by using a fine mesh containing sixty B22 elements (B22 is the 3-node quadratic beam element of Abaqus [5]). The load-displacement curves of US-ATFQ4 compared with CPS4, CPS4I are plotted in Figure 18.

Similar to the previous examples, the results obtained by CPS4I agree well with the reference solutions only for the regular mesh. But the present element US-ATFQ4 performs very well for both regular and distorted meshes. So, it is clear that the present new formulations also exhibit excellent performance in predicting the snapback instability of the Lee's frame by employing the modified Riks method. Four deformed states of the frame corresponding to states I, II, III and IV in Figure 18 obtained by US-ATFQ4 with twenty-five distorted elements are shown in Figure 19.

Besides, this example is redone with a non-zero Poisson's ratio,  $\mu=0.3$ . The resulting load-displacement curves of US-ATFQ4 compared with CPS4, CPS4I are given in Figure 20. The situation is the same as that with zero Poisson's ratio.

## 5. CONCLUSIONS REMARKS

An approach to develop a 4-node, 8-DOF plane quadrilateral finite element model with high precision and high distortion tolerance, for both linear and nonlinear problems, has been attracting many researchers for a long time. Unfortunately, due to some inherent defects, it is almost an impossible mission, just like the contradiction defined by MacNeal's theorem [28, 29].

Recently, a breakthrough was achieved for linear elastic problems. A series of 2D and 3D unsymmetric finite element models with analytical trial functions were successfully constructed [30, 51, 52]. These elements contain the analytical solutions for homogeneous control equations of linear

elasticity, and exhibit excellent precision for both regular and severely distorted meshes. Especially, the 4-node, 8-DOF plane quadrilateral element US-ATFQ4 [30] and the 8-node, 24-DOF 3D hexahedral element US-ATFH8 [52] can completely break through the limitation given by MacNeal's theorem. However, it should be noted that these successes must depend on the general solutions of linear elasticity. Once there are no such solutions, for example, nonlinear problems, could anyone find an effective way to keep the same performance? Therefore, how to modify original formulations into incremental forms for nonlinear applications and design an appropriate updated algorithm become the key of the whole job.

In this paper, the unsymmetric 4-node, 8-DOF plane element US-ATFQ4 [30] is extended to geometric nonlinear analysis. First, the analytical trial functions should be updated at each iterative step in the framework of updated Lagrangian (UL) formulation that takes the current configuration, i.e. the configurations at the beginning of an incremental step, as the reference configuration during that step. Second, an appropriate stress update algorithm in which the Cauchy stresses are updated by the Hughes-Winget method [34] is adopted to estimate current stress field. Numerical examples show that the new nonlinear element US-ATFQ4 also possesses amazing performance for geometric nonlinear analysis, no matter regular or distorted meshes are used. It again demonstrates the advantages of the unsymmetric finite element method with analytical trial functions, although these functions only come from linear elasticity.

This is the first attempt to generalize the finite element model with the analytical trial functions of linear elasticity to nonlinear application, and only the small strain with large displacement/rotation problems are concerned. Since a rate form of updating algorithm is adopted, the formulations can be straightforward extended to large deformation problems. This topic will be discussed in another paper in the near future.

## APPENDIX A. THE SECOND FORM OF QUADRILATERAL AREA COORDINATES (QACM-II) [24]

As shown in Figure A,  $M_i$  ( $i=1,2,3,4$ ) are the mid-side points of element edges  $\overline{23}$ ,  $\overline{34}$ ,  $\overline{41}$  and  $\overline{12}$ , respectively. Then, the position of an arbitrary point P within the quadrilateral element  $\overline{1234}$  can be uniquely specified by the area coordinates  $S$  and  $T$  (QACM-II), which are defined as:

$$S = 4 \frac{\Omega_1}{A}, \quad T = 4 \frac{\Omega_2}{A}, \quad (\text{A.1})$$

where  $A$  is the area of the quadrilateral element;  $\Omega_1$  and  $\Omega_2$  are the *generalized areas* of  $\Delta PM_2M_4$  and  $\Delta PM_3M_1$ , respectively. The values of *generalized areas*  $\Omega_1$  and  $\Omega_2$  can be both positive and negative: for  $\Delta PM_2M_4$  (or  $\Delta PM_3M_1$ ), if the permutation order of points P,  $M_2$  and  $M_4$  (or P,  $M_3$  and  $M_1$ ) is anticlockwise, a positive  $\Omega_1$  (or  $\Omega_2$ ) should be taken; otherwise,  $\Omega_1$  (or  $\Omega_2$ ) should be negative.

Two shape parameters  $\bar{g}_1$  and  $\bar{g}_2$  are defined here as:

$$\begin{cases} \bar{g}_1 = \frac{A_{\Delta 123} - A_{\Delta 124}}{A} \\ \bar{g}_2 = \frac{A_{\Delta 234} - A_{\Delta 123}}{A} = \frac{A - A_{\Delta 124} - A_{\Delta 123}}{A} \end{cases}, \quad (\text{A.2})$$

in which  $A_{\Delta 123}$ ,  $A_{\Delta 124}$  and  $A_{\Delta 234}$  are the areas of  $\Delta 123$ ,  $\Delta 124$  and  $\Delta 234$ , respectively. Different values of these shape parameters mean different shapes of a quadrangle. Thus, the local coordinates of the corner nodes and mid-side points can be written as:

$$\begin{aligned} \text{node 1: } (S_1, T_1) &= (-1 + \bar{g}_2, -1 + \bar{g}_1); & \text{node 2: } (S_2, T_2) &= (1 - \bar{g}_2, 1 - \bar{g}_1); \\ \text{node 3: } (S_3, T_3) &= (1 + \bar{g}_2, 1 + \bar{g}_1); & \text{node 4: } (S_4, T_4) &= (-1 - \bar{g}_2, -1 - \bar{g}_1); \\ M_1 &: (1, 0); & M_2 &: (0, 1); \\ M_3 &: (-1, 0); & M_4 &: (0, -1). \end{aligned} \quad (\text{A.3})$$

Above coordinate values are only small modifications for isoparametric coordinates:

$$\begin{cases} S = \xi + \bar{g}_2 \xi \eta \\ T = \eta + \bar{g}_1 \xi \eta \end{cases}. \quad (\text{A.4})$$

And the relationship between QACM-II and the Cartesian coordinates is

$$\begin{cases} S = \frac{1}{A}[(a_3 - a_1) + (b_3 - b_1)x + (c_3 - c_1)y] + \bar{g}_1 = \frac{1}{A}[\bar{a}_1 + \bar{b}_1x + \bar{c}_1y] + \bar{g}_1 \\ T = \frac{1}{A}[(a_4 - a_2) + (b_4 - b_2)x + (c_4 - c_2)y] + \bar{g}_2 = \frac{1}{A}[\bar{a}_2 + \bar{b}_2x + \bar{c}_2y] + \bar{g}_2 \end{cases}, \quad (\text{A.5})$$

where

$$\begin{cases} \bar{a}_1 = a_3 - a_1, & \bar{b}_1 = b_3 - b_1, & \bar{c}_1 = c_3 - c_1, \\ \bar{a}_2 = a_4 - a_2, & \bar{b}_2 = b_4 - b_2, & \bar{c}_2 = c_4 - c_2, \end{cases} \quad (\text{A.6})$$

$$\begin{aligned} a_i = x_j y_k - x_k y_j, \quad b_i = y_j - y_k, \quad c_i = x_k - x_j, \\ (i = 1, 2, 3, 4; \quad j = 2, 3, 4, 1; \quad k = 3, 4, 1, 2) \end{aligned} \quad (\text{A.7})$$

in which  $(x_i, y_i)$  ( $i=1, 2, 3, 4$ ) are the Cartesian coordinates of the four corner nodes.

## APPENDIX B. THE EXPRESSIONS OF $[\hat{\mathbf{N}}]$ IN EQUATION (14)

${}^tU_7$ ,  ${}^tV_7$ ,  ${}^tU_8$  and  ${}^tV_8$  in equation (11) are the linear displacement solutions or plane pure bending in arbitrary direction and referred to configuration  $C_1$ . For isotropic case, they can be written as [29]

$$\begin{cases} {}^tU_7 = \frac{3}{16E'A^3}[(4\bar{c}_1^2\bar{c}_2A - \bar{c}_1^2\bar{b}_2f_3 - \bar{b}_1\bar{b}_2^2f_1 - 16\bar{b}_1\mu'A^2) {}^tS^2 + 2\bar{b}_2f_1^2 {}^tS {}^tT - \bar{b}_1f_1^2 {}^tT^2] \\ {}^tV_7 = \frac{3}{16E'A^3}[(-4\bar{b}_1^2\bar{b}_2A - \bar{b}_1^2\bar{c}_2f_3 - \bar{c}_1\bar{c}_2^2f_1 - 16\bar{c}_1\mu'A^2) {}^tS^2 + 2\bar{c}_2f_1^2 {}^tS {}^tT - \bar{c}_1f_1^2 {}^tT^2] \end{cases}, \quad (\text{B.1})$$

$$\begin{cases} {}^tU_8 = \frac{3}{16E'A^3}[-\bar{b}_2f_2^2 {}^tS^2 + 2\bar{b}_1f_2^2 {}^tS {}^tT - (4\bar{c}_2^2\bar{c}_1A + \bar{c}_2^2\bar{b}_1f_3 + \bar{b}_2\bar{b}_1^2f_2 + 16\bar{b}_2\mu'A^2) {}^tT^2] \\ {}^tV_8 = \frac{3}{16E'A^3}[-\bar{c}_2f_2^2 {}^tS^2 + 2\bar{c}_1f_2^2 {}^tS {}^tT - (-4\bar{b}_2^2\bar{b}_1A + \bar{b}_2^2\bar{c}_1f_3 + \bar{c}_2\bar{c}_1^2f_2 + 16\bar{c}_2\mu'A^2) {}^tT^2] \end{cases}, \quad (\text{B.2})$$

where  ${}^tS$  and  ${}^tT$  are the quadrilateral area coordinates at time  $t$ .

And  $[\hat{\mathbf{N}}]$  in equation (14) can be rewritten as [29]:

$$[\hat{\mathbf{N}}] = [\mathbf{P}][\hat{\mathbf{d}}]^{-1}, \quad (\text{B.3})$$

where

$$\begin{bmatrix} {}^t\hat{\mathbf{d}} \end{bmatrix} = \begin{bmatrix} \mathbf{P}({}^t x_1, {}^t y_1, {}^t S_1, {}^t T_1) \\ \mathbf{P}({}^t x_2, {}^t y_2, {}^t S_2, {}^t T_2) \\ \mathbf{P}({}^t x_3, {}^t y_3, {}^t S_3, {}^t T_3) \\ \mathbf{P}({}^t x_4, {}^t y_4, {}^t S_4, {}^t T_4) \end{bmatrix} = \begin{bmatrix} 1 & 0 & {}^t x_1 & 0 & {}^t y_1 & 0 & U_7({}^t S_1, {}^t T_1) & U_8({}^t S_1, {}^t T_1) \\ 0 & 1 & 0 & {}^t x_1 & 0 & {}^t y_1 & V_7({}^t S_1, {}^t T_1) & V_8({}^t S_1, {}^t T_1) \\ 1 & 0 & {}^t x_2 & 0 & {}^t y_2 & 0 & U_7({}^t S_2, {}^t T_2) & U_8({}^t S_2, {}^t T_2) \\ 0 & 1 & 0 & {}^t x_2 & 0 & {}^t y_2 & V_7({}^t S_2, {}^t T_2) & V_8({}^t S_2, {}^t T_2) \\ 1 & 0 & {}^t x_3 & 0 & {}^t y_3 & 0 & U_7({}^t S_3, {}^t T_3) & U_8({}^t S_3, {}^t T_3) \\ 0 & 1 & 0 & {}^t x_3 & 0 & {}^t y_3 & V_7({}^t S_3, {}^t T_3) & V_8({}^t S_3, {}^t T_3) \\ 1 & 0 & {}^t x_4 & 0 & {}^t y_4 & 0 & U_7({}^t S_4, {}^t T_4) & U_8({}^t S_4, {}^t T_4) \\ 0 & 1 & 0 & {}^t x_4 & 0 & {}^t y_4 & V_7({}^t S_4, {}^t T_4) & V_8({}^t S_4, {}^t T_4) \end{bmatrix}, \quad (\text{B.3})$$

in which  $({}^t x_I, {}^t y_I), ({}^t S_I, {}^t T_I)$  are, respectively, the Cartesian coordinates and quadrilateral area coordinates (QACM-II) of the four corner nodes ( $I=1,2,3,4$ ) at time  $t$ ; and  $[\mathbf{P}]$  has been given by equation (11).

## ACKNOWLEDGEMENTS

The authors would like to thank for the financial supports from the National Natural Science Foundation of China (11272181, 11702133), the Tsinghua University Initiative Scientific Research Program (2014z09099) and the Natural Science Foundation of Jiangsu Province (BK20170772).

## REFERENCES

1. Zienkiewicz OC, Taylor RL, Zhu JZ. *The Finite Element Method: Its Basis and Fundamentals*. 7th ed. Oxford: Butterworth-Heinemann; 2013.
2. Long YQ, Cen S, Long ZF. *Advanced Finite Element Method in Structural Engineering*. Berlin, Heidelberg: Springer-Verlag GmbH; Beijing: Tsinghua University Press; 2009.
3. Wilson EL, Taylor RL, Doherty WP, Ghaboussi J. Incompatible displacement models. In: Fenves SJ, et al., ed. *Numerical and Computer Methods in Structural Mechanics*. New York: Academic Press; 1973: 43-57.
4. Taylor RL, Beresford PJ, Wilson EL. A non-conforming element for stress analysis. *International Journal for Numerical Methods in Engineering* 1976;10(6):1211-1219.
5. *Abaqus 2017 Documentation*. Providence, RI, USA: Dassault Systèmes Simulia Corp.; 2016.
6. Simo JC, Rifai MS. A class of mixed assumed strain methods and the method of incompatible modes. *International Journal for Numerical Methods in Engineering* 1990;29(8):1595-1638.
7. Pian THH, Sumihara K. Rational approach for assumed stress finite-elements. *International Journal for Numerical Methods in Engineering* 1984;20(9):1685-1695.
8. Wu CC, Huang MG, Pian THH. Consistency condition and convergence criteria of incompatible elements: general formulation of incompatible functions and its application. *Computers & Structures* 1987;27(5):639-644.
9. Yeo ST, Lee BC. New stress assumption for hybrid stress elements and refined four-node plane and eight-node brick elements. *International Journal for Numerical Methods in Engineering* 1997;40(16):2933-2952.
10. Sze KY. On immunizing five-beta hybrid-stress element models from ‘trapezoidal locking’ in practical analyses. *International Journal for Numerical Methods in Engineering* 2000;47(4):907-920.
11. Pian THH, Wu CC. *Hybrid and incompatible finite element methods*. Boca Raton: Chapman & Hall/CRC; 2006.
12. Cen S, Zhang T, Li C-F, Fu X-R, Long Y-Q. A hybrid-stress element based on Hamilton principle. *Acta Mechanica Sinica* 2010;26(4):625-634.
13. Chen WJ, Tang LM. Isoparametric quasi-conforming element. *Journal of Dalian University of Technology* 1981;20(1):63-74 (in Chinese).
14. Piltner R, Taylor RL. A quadrilateral mixed finite-element with two enhanced strain modes. *International Journal for Numerical Methods in Engineering* 1995;38(11):1783-1808.
15. Korelc J, Wriggers P. Improved enhanced strain four-node element with Taylor expansion of the shape functions. *International Journal for Numerical Methods in Engineering* 1997;40(3):407-421.
16. Lautersztajn-S N, Samuelsson A. Further discussion on four-node isoparametric quadrilateral elements in plane bending. *International Journal for Numerical Methods in Engineering* 2000;47(1-3):129-140.
17. Piltner R, Taylor RL. A systematic construction of B-bar functions for linear and non-linear mixed-enhanced finite elements for plane elasticity problems. *International Journal for Numerical Methods in Engineering* 1999;44(5):615-639.

18. Long YQ, Li JX, Long ZF, Cen S. Area co-ordinates used in quadrilateral elements. *Communications in Numerical Methods in Engineering* 1999;15(8):533-545.
19. Long ZF, Li JX, Cen S, Long YQ. Some basic formulae for area co-ordinates in quadrilateral elements. *Communications in Numerical Methods in Engineering* 1999;15(12):841-852.
20. Chen XM, Cen S, Long YQ, Yao ZH. Membrane elements insensitive to distortion using the quadrilateral area coordinate method. *Computers & Structures* 2004;82(1):35-54.
21. Cen S, Chen XM, Fu XR. Quadrilateral membrane element family formulated by the quadrilateral area coordinate method. *Computer Methods in Applied Mechanics and Engineering* 2007;196(41):4337-4353.
22. Cen S, Du Y, Chen XM, Fu XR. The analytical element stiffness matrix of a recent 4-node membrane element formulated by the quadrilateral area co-ordinate method. *Communications in Numerical Methods in Engineering* 2007;23(12):1095-1110.
23. Du Y, Cen S. Geometrically nonlinear analysis with a 4-node membrane element formulated by the quadrilateral area coordinate method. *Finite Elements in Analysis and Design* 2008;44(8):427-438.
24. Chen XM, Cen S, Fu XR, Long YQ. A new quadrilateral area coordinate method (QACM-II) for developing quadrilateral finite element models. *International Journal for Numerical Methods in Engineering* 2008;73(13):1911-1941.
25. Cen S, Chen XM, Li CF, Fu XR. Quadrilateral membrane elements with analytical element stiffness matrices formulated by the new quadrilateral area coordinate method (QACM-II). *International Journal for Numerical Methods in Engineering* 2009;77(8):1172-1200.
26. Long ZF, Cen S, Wang L, Fu XR, Long YQ. The third form of the quadrilateral area coordinate method (QACM-III): Theory, application, and scheme of composite coordinate interpolation. *Finite Elements in Analysis and Design* 2010;46(10):805-818.
27. Li G. A four-node plane parametric element based on quadrilateral area coordinate and its application to coupled solid-deformation/fluid-flow simulation for porous geomaterials. *International Journal for Numerical and Analytical Methods in Geomechanics* 2015;39(3):251-276.
28. Macneal RH. A theorem regarding the locking of tapered four-noded membrane elements. *International Journal for Numerical Methods in Engineering* 1987;24(9):1793-1799.
29. Macneal RH. On the limits of finite element perfectability. *International Journal for Numerical Methods in Engineering* 1992;35(8):1589-1601.
30. Cen S, Zhou PL, Li CF, Wu CJ. An unsymmetric 4-node, 8-DOF plane membrane element perfectly breaking through MacNeal's theorem. *International Journal for Numerical Methods in Engineering* 2015;103(7):469-500.
31. Rajendran S, Liew KM. A novel unsymmetric 8-node plane element immune to mesh distortion under a quadratic displacement field. *International Journal for Numerical Methods in Engineering* 2003;58(11):1713-1748.
32. Felippa CA, Haugen B. A unified formulation of small-strain corotational finite elements: I. Theory. *Computer Methods in Applied Mechanics and Engineering* 2005;194(21-24):2285-2335.

33. Belytschko T, Liu W, Moran B, Elkhodary KI. *Nonlinear Finite Elements for Continua and Structures*. 2nd ed. Chichester, UK: John Wiley & Sons 2014.
34. Hughes TJR, Winget J. Finite rotation effects in numerical integration of rate constitutive equations arising in large-deformation analysis. *International Journal for Numerical Methods in Engineering* 1980;15(12):1862-1867.
35. Rashid M. Incremental kinematics for finite element applications. *International journal for numerical methods in engineering* 1993;36(23):3937-3956.
36. Simo J, Hughes TJ. *Computational inelasticity*. New York: Springer-Verlag; 1998.
37. Wang C, Zhang X, Hu P, Qi Z. Linear and geometrically nonlinear analysis with 4-node plane quasi-conforming element with internal parameters. *Acta Mechanica Solida Sinica* 2015;28(6):668-681.
38. Ko Y, Lee P-S, Bathe K-J. A new 4-node MITC element for analysis of two-dimensional solids and its formulation in a shell element. *Computers & Structures* 2017;192:34-49.
39. Wisniewski K, Turska E. Improved 4-node Hu–Washizu elements based on skew coordinates. *Computers & Structures* 2009;87(7):407-424.
40. Wisniewski K, Wagner W, Turska E, Gruttmann F. Four-node Hu–Washizu elements based on skew coordinates and contravariant assumed strain. *Computers & Structures* 2010;88(21):1278-1284.
41. Zouari W, Hammadi F, Ayad R. Quadrilateral membrane finite elements with rotational DOFs for the analysis of geometrically linear and nonlinear plane problems. *Computers & Structures* 2016;173:139-149.
42. Wulfinghoff S, Bayat HR, Alipour A, Reese S. A low-order locking-free hybrid discontinuous Galerkin element formulation for large deformations. *Computer Methods in Applied Mechanics and Engineering* 2017;323:353-372.
43. Rajendran S, Zhang BR, Liew KM. A partition of unity-based ‘FE-meshfree’ QUAD4 element for geometric non-linear analysis. *International Journal for Numerical Methods in Engineering* 2010;82(12):1574-1608.
44. Cowan T, Coombs WM. Rotationally invariant distortion resistant finite-elements. *Computer Methods in Applied Mechanics and Engineering* 2014;275:189-203.
45. De Borst R, Crisfield MA, Remmers JJ, Verhoosel CV. *Non-linear Finite Element Analysis of Solids and Structures*. 2nd ed. Chichester, UK: John Wiley & Sons; 2012.
46. Bathe KJ. *Finite Element Procedures*. 2nd ed. Watertown, MA: K.J. Bathe; 2014.
47. Battini JM. A non-linear corotational 4-node plane element. *Mechanics Research Communications* 2008;35(6):408-413.
48. Fredriksson M, Ottosen NS. Fast and accurate 4-node quadrilateral. *International Journal for Numerical Methods in Engineering* 2004;61(11):1809-1834.
49. Sze KY, Liu XH, Lo SH. Popular benchmark problems for geometric nonlinear analysis of shells. *Finite Elements in Analysis and Design* 2004;40(11):1551-1569.
50. Lyons P, Holsgrove S. *Finite Element Benchmarks For 2D Beams And Axisymmetric Shells Involving Geometric Non-Linearity*. NAFEMS; 1989.

51. Cen S, Zhou GH, Fu XR. A shape-free 8-node plane element unsymmetric analytical trial function method. *International Journal for Numerical Methods in Engineering* 2012;91(2):158-185.
52. Zhou PL, Cen S, Huang JB, Li CF, Zhang Q. An unsymmetric 8-node hexahedral element with high distortion tolerance. *International Journal for Numerical Methods in Engineering* 2017;109(8):1130-1158.

Table I. The number of increments NINC and iterations NITER required to obtain the converged ultimate solutions for the slender cantilever beam subjected to an end resultant shear force problem (Figure 5).

(a)  $1 \times 10$  regular mesh

Mesh (a)	CPE4	CPE4I	CPE4R	CPE8	US-ATFQ4
NINC	6	9	11	10	10
NITER	7	43	52	51	50

(b)  $1 \times 10$  distorted mesh

Mesh (b)	CPE4	CPE4I	CPE4R	CPE8	US-ATFQ4
NINC	6	6	6	9	10
NITER	7	7	7	42	55

Table II. Results of vertical and horizontal tip displacements for the slender cantilever beam subjected to an end resultant shear force (Figure 5), fixed time increment 0.1.

(a)  $1 \times 10$  regular mesh

Mesh (a)		$V_{\text{Tip}}$				$U_{\text{Tip}}$			
Total time	CPE4I	CPE8	US-ATFQ4	Reference [49]	CPE4I	CPE8	US-ATFQ4	Reference [49]	
0.0	0.0000	0.0000	<b>0.0000</b>	0.0000	0.0000	0.0000	<b>0.0000</b>	0.0000	
0.1	1.2985	1.2976	<b>1.3069</b>	1.3086	-0.1018	-0.1016	<b>-0.1029</b>	-0.1033	
0.2	2.4558	2.4562	<b>2.4907</b>	2.4926	-0.3704	-0.3701	<b>-0.3799</b>	-0.3808	
0.3	3.4101	3.4132	<b>3.4874</b>	3.4879	-0.7316	-0.7308	<b>-0.7616</b>	-0.7626	
0.4	4.1701	4.1755	<b>4.2937</b>	4.2919	-1.1234	-1.1208	<b>-1.1838</b>	-1.1840	
0.5	4.7732	4.7778	<b>4.9371</b>	4.9325	-1.5113	-1.5038	<b>-1.6055</b>	-1.6040	
0.6	5.2517	5.2567	<b>5.4507</b>	5.4436	-1.8759	-1.8633	<b>-2.0054</b>	-2.0020	
0.7	5.6361	5.6422	<b>5.8646</b>	5.8550	-2.2117	-2.1937	<b>-2.3753</b>	-2.3696	
0.8	5.9490	5.9570	<b>6.2016</b>	6.1903	-2.5176	-2.4947	<b>-2.7128</b>	-2.7050	
0.9	6.2071	6.2175	<b>6.4829</b>	6.4670	-2.7952	-2.7680	<b>-3.0232</b>	-3.0098	
1.0	6.4227	6.4362	<b>6.7146</b>	6.6984	-3.0471	-3.0162	<b>-3.3005</b>	-3.2863	

(b)  $1 \times 10$  distorted mesh

Mesh (b)		$V_{\text{Tip}}$				$U_{\text{Tip}}$			
Total time	CPE4I	CPE8	US-ATFQ4	Reference [49]	CPE4I	CPE8	US-ATFQ4	Reference [49]	
0.0	0.0000	0.0000	<b>0.0000</b>	0.0000	0.0000	0.0000	<b>0.0000</b>	0.0000	
0.1	0.0136	1.1990	<b>1.3198</b>	1.3086	0.0000	-0.0868	<b>-0.1048</b>	-0.1033	
0.2	0.0272	2.2886	<b>2.5279</b>	2.4926	0.0000	-0.3206	<b>-0.3906</b>	-0.3808	
0.3	0.0407	3.2091	<b>3.5556</b>	3.4879	-0.0001	-0.6428	<b>-0.7902</b>	-0.7626	
0.4	0.0541	3.9579	<b>4.3932</b>	4.2919	-0.0002	-0.9996	<b>-1.2376</b>	-1.1840	
0.5	0.0675	4.5597	<b>5.0643</b>	4.9325	-0.0002	-1.3571	<b>-1.6883</b>	-1.6040	
0.6	0.0808	5.0448	<b>5.6010</b>	5.4436	-0.0003	-1.6979	<b>-2.1182</b>	-2.0020	
0.7	0.0941	5.4393	<b>6.0338</b>	5.8550	-0.0005	-2.0151	<b>-2.5176</b>	-2.3696	
0.8	0.1073	5.7640	<b>6.3855</b>	6.1903	-0.0006	-2.3069	<b>-2.8821</b>	-2.7050	
0.9	0.1204	6.0303	<b>6.6761</b>	6.4670	-0.0007	-2.5691	<b>-3.2144</b>	-3.0098	
1.0	0.1335	6.2617	<b>6.9209</b>	6.6984	-0.0009	-2.8169	<b>-3.5190</b>	-3.2863	

Table III. The number of increments NINC and iterations NITER required to obtain the converged ultimate solutions for the slender cantilever beam subjected to an end resultant moment (Figure 10).

(a)  $1 \times 10$  regular mesh

Mesh (a)	CPE4	CPE4I	CPE4R	CPE8	US-ATFQ4
NINC	6	44	39	36	34
NITER	8	264	222	220	203

(b)  $1 \times 20$  distorted mesh

Mesh (b)	CPE4	CPE4I	CPE4R	CPE8	US-ATFQ4
NINC	6	6	6	49	41
NITER	8	13	12	313	223

Table IV. Vertical and horizontal tip displacements for the slender cantilever beam subjected to an end resultant moment (Figure 10), fixed time increment 0.01.

(a)  $1 \times 10$  regular mesh

Mesh (a)		$V_{\text{Tip}}$			$U_{\text{Tip}}$			
Total time	CPE4I	CPE8	US-ATF Q4	Reference [49]	CPE4I	CPE8	US-ATF Q4	Reference [49]
0.0	0.0000	0.0000	<b>0.0000</b>	0.0000	0.0000	0.0000	<b>0.0000</b>	0.0000
0.1	3.6124	3.5855	<b>3.6499</b>	3.6480	-0.7599	-0.7466	<b>-0.7730</b>	-0.7740
0.2	6.4381	6.2884	<b>6.6136</b>	6.5980	-2.7802	-2.5894	<b>-2.9235</b>	-2.9180
0.3	8.0804	7.8849	<b>8.3626</b>	8.3330	-5.5003	-4.8229	<b>-5.9843</b>	-5.9450
0.4	8.4920	8.5854	<b>8.6499</b>	8.6370	-8.3130	-6.9802	<b>-9.2977</b>	-9.1940
0.5	7.8923	8.6725	<b>7.5698</b>	7.6390	-10.7363	-8.8636	<b>-12.1711</b>	-12.0000
0.6	6.6380	8.3712	<b>5.5375</b>	5.7580	-12.4912	-10.4223	<b>-14.0474</b>	-13.8710
0.7	5.1014	7.8383	<b>3.1869</b>	3.5710	-13.5012	-11.6679	<b>-14.6504</b>	-14.5950
0.8	3.5882	7.1785	<b>1.2019</b>	1.6500	-13.8405	-12.6349	<b>-14.0673</b>	-14.2700
0.9	2.3019	6.4606	<b>0.1167</b>	0.4050	-13.6666	-13.3628	<b>-12.7371</b>	-13.2470
1.0	1.3454	5.7298	<b>0.1346</b>	0.0000	-13.1618	-13.8897	<b>-11.3299</b>	-12.0000

(b)  $1 \times 20$  distorted mesh

Mesh (b)		$V_{\text{Tip}}$			$U_{\text{Tip}}$			
Total time	CPE4I	CPE8	US-ATF Q4	Reference [49]	CPE4I	CPE8	US-ATF Q4	Reference [49]
0.0	0.0000	0.0000	<b>0.0000</b>	0.0000	0.0000	0.0000	<b>0.0000</b>	0.0000
0.1	0.1379	3.6050	<b>3.6518</b>	3.6480	-0.0010	-0.7549	<b>-0.7754</b>	-0.7740
0.2	0.2746	6.5185	<b>6.6171</b>	6.5980	-0.0038	-2.8274	<b>-2.9349</b>	-2.9180
0.3	0.4101	8.2617	<b>8.3607</b>	8.3330	-0.0086	-5.7143	<b>-6.0119</b>	-5.9450
0.4	0.5447	8.6870	<b>8.6274</b>	8.6370	-0.0151	-8.7768	<b>-9.3436</b>	-9.1940
0.5	0.6784	7.9684	<b>7.5067</b>	7.6390	-0.0236	-11.4502	<b>-12.2242</b>	-12.0000
0.6	0.8113	6.4825	<b>5.4198</b>	5.7580	-0.0338	-13.3680	<b>-14.0777</b>	-13.8710
0.7	0.9437	4.6721	<b>3.0234</b>	3.5710	-0.0460	-14.3997	<b>-14.6113</b>	-14.5950
0.8	1.0751	2.9233	<b>1.0432</b>	1.6500	-0.0600	-14.6201	<b>-13.9134</b>	-14.2700
0.9	1.2064	1.5037	<b>0.0618</b>	0.4050	-0.0759	-14.2284	<b>-12.4629</b>	-13.2470
1.0	1.3367	0.5466	<b>0.3028</b>	0.0000	-0.0937	-13.4710	<b>-11.0282</b>	-12.0000

Table V. The number of increments NINC and iterations NITER required to obtain the converged ultimate solutions for the angle frame problem (Figure 14).

(a) Regular mesh with 7 rectangular elements

Mesh (a)	CPS4	CPS4I	US-ATFQ4
NINC	6	6	8
NITER	12	26	31

(b) Distorted mesh with 19 distorted elements

Mesh (b)	CPS4	CPS4I	US-ATFQ4
NINC	6	7	7
NITER	18	27	27

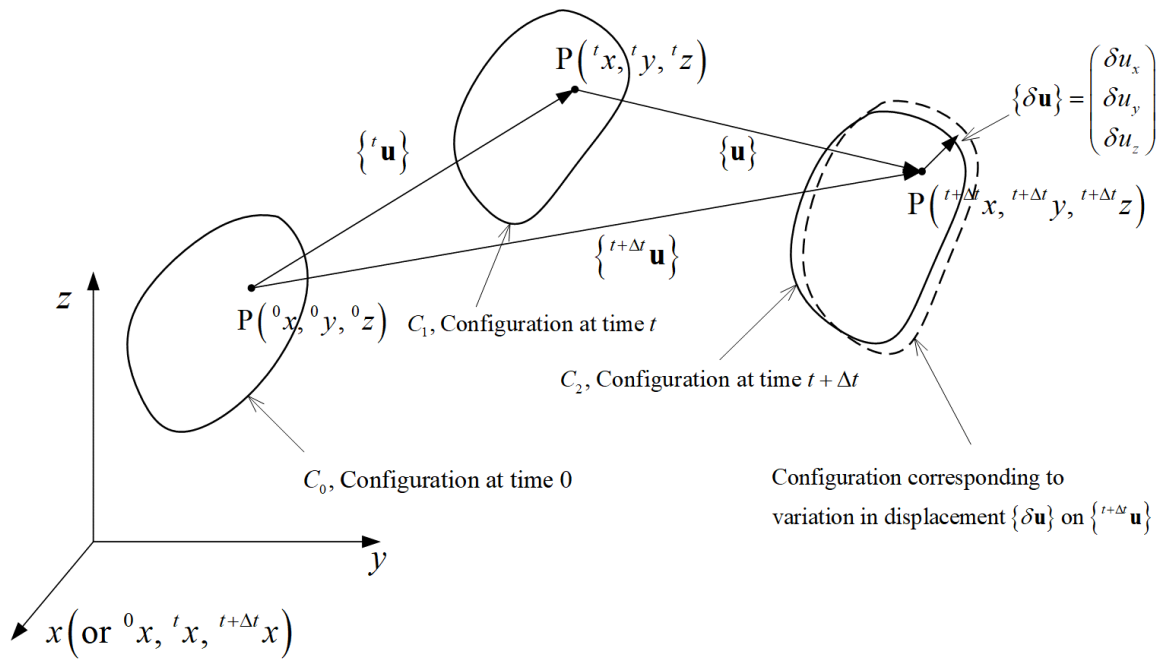


Figure 1. Large displacement motion of a body in Cartesian coordinate system.

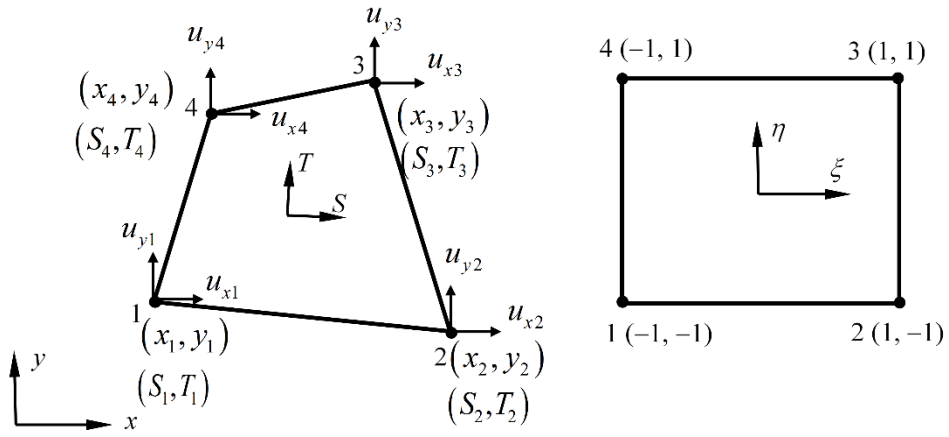


Figure 2. A 4-node plane quadrilateral element.

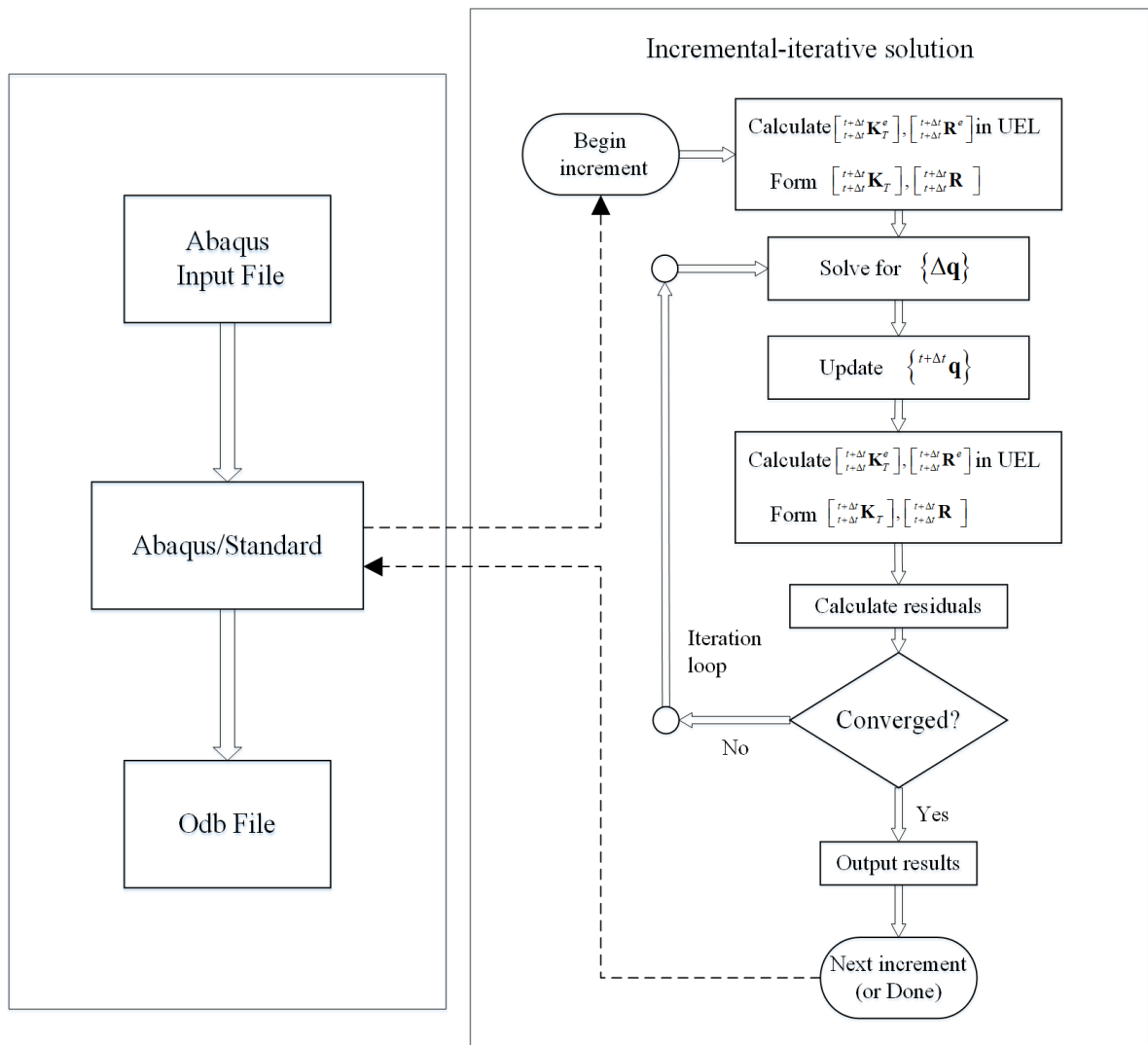


Figure 3. The incremental-iterative Newton-Raphson scheme in Abaqus/Standard.

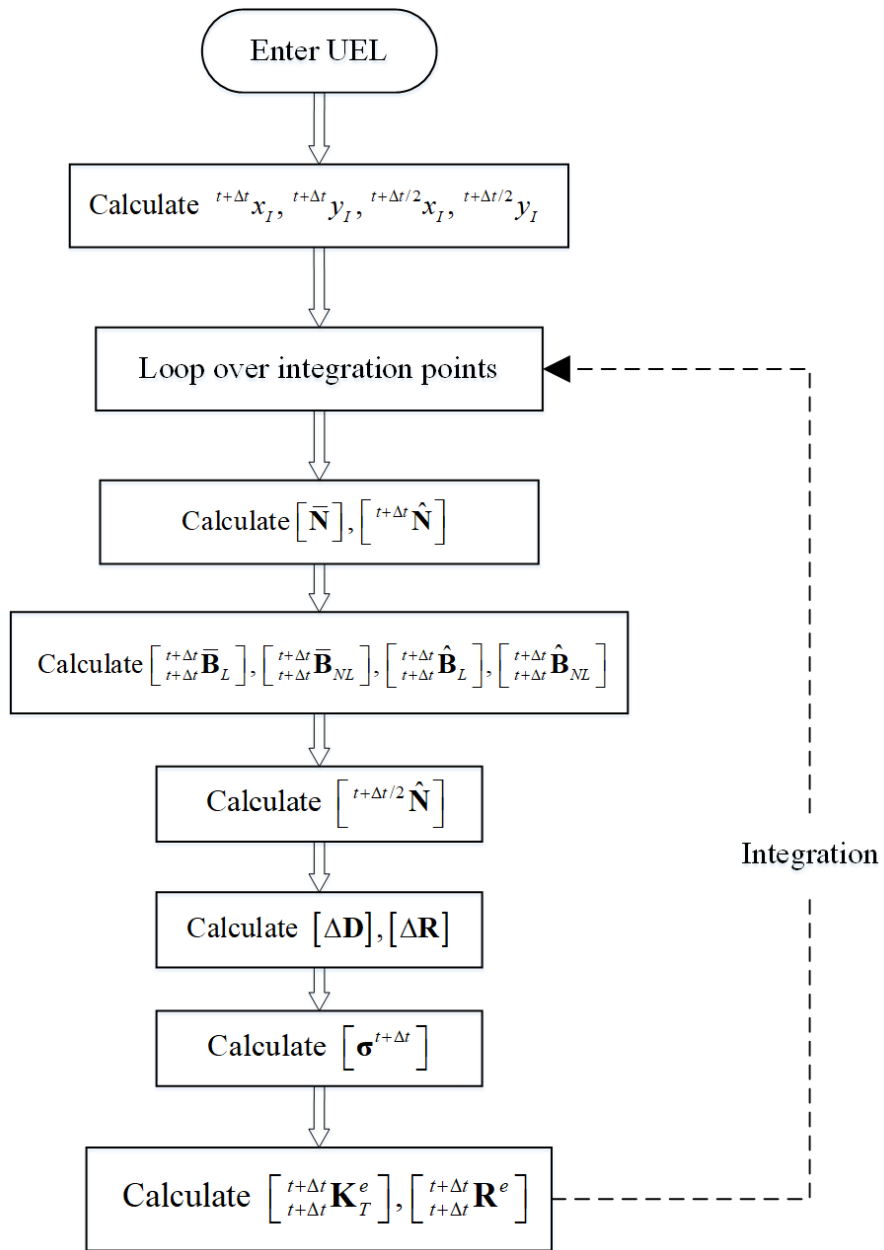


Figure 4. The computation flowchart of the nonlinear formulations of element US-ATFQ4.

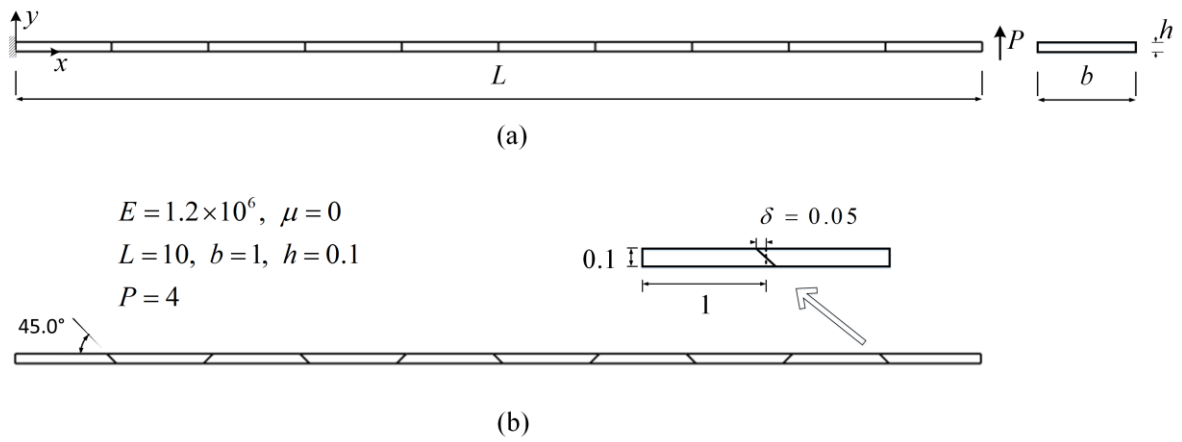
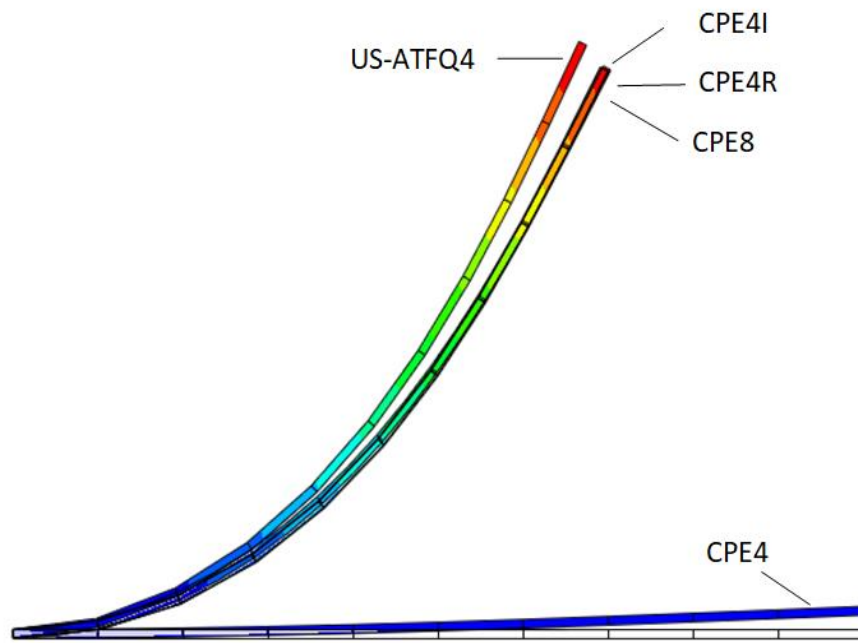
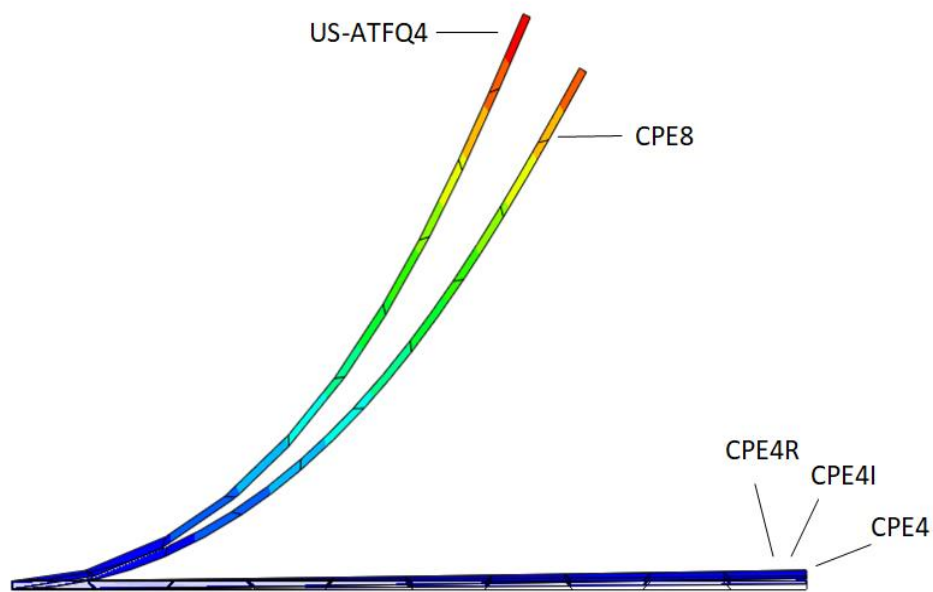


Figure 5. A slender cantilever beam subjected to end resultant shear force and two mesh cases.  
 (a) Regular mesh; (b) Distorted mesh.

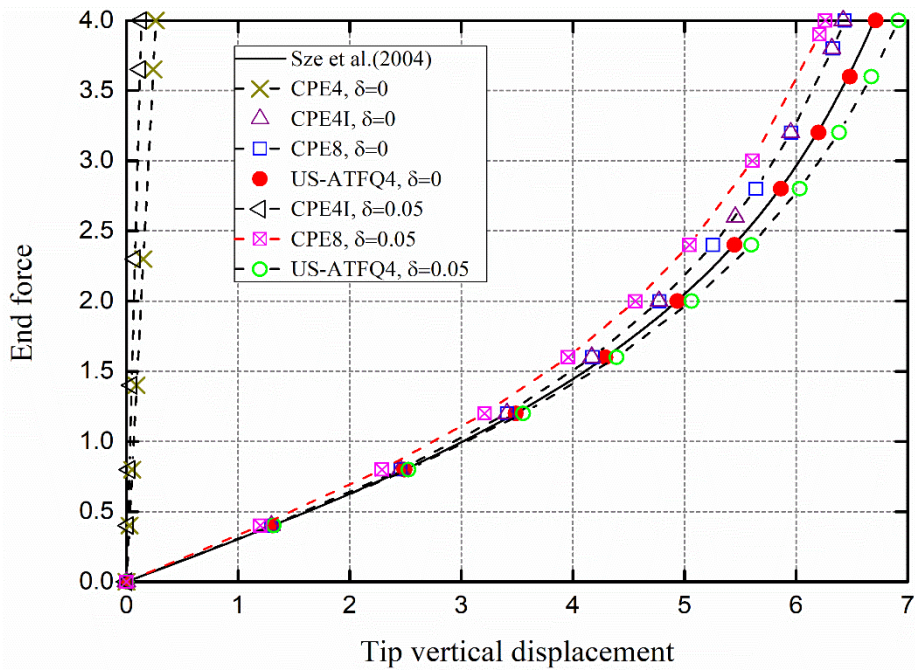


(a) Results obtained by  $1 \times 10$  regular rectangle elements;

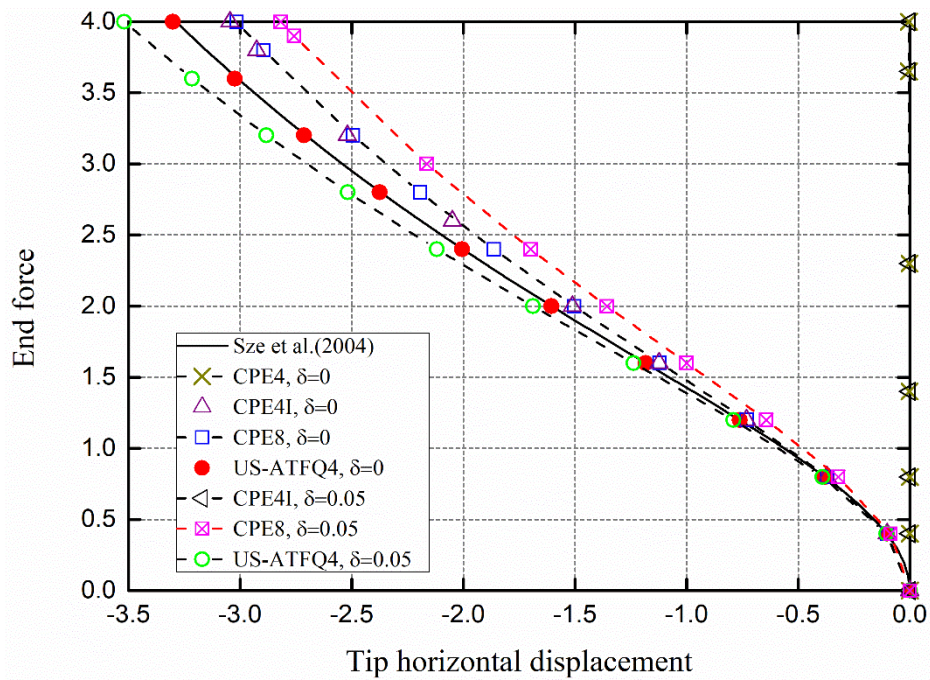


(b) Results obtained by  $1 \times 10$  distorted elements.

Figure 6. The deformed shapes of slender cantilever beam subjected to end resultant shear force.

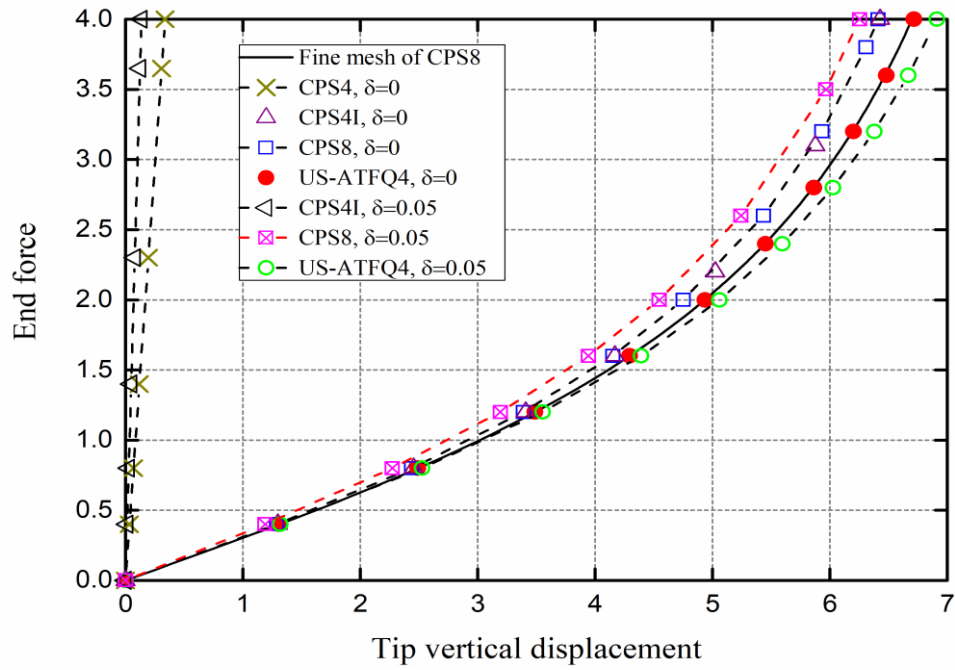


(a) End shear force versus vertical displacement curves,  
 $1 \times 10$  regular and distorted mesh;

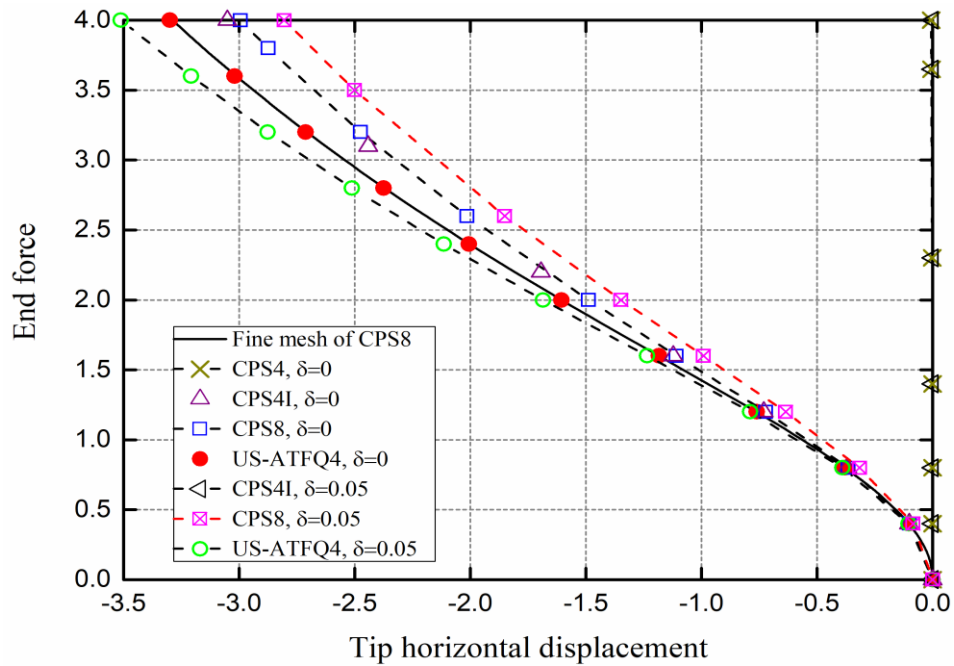


(b) End shear force versus horizontal displacement curves,  
 $1 \times 10$  regular and distorted mesh.

Figure 7. Load-displacement curves for a slender cantilever beam subjected to an end resultant shear force with  $\mu=0$  (Example 4.1).



(a) End shear force versus vertical displacement curves,  $1 \times 10$  regular and distorted mesh;



(b) End shear force versus horizontal displacement curves,  $1 \times 10$  regular and distorted mesh.

Figure 8. Load-displacement curves for a slender cantilever beam subjected to an end resultant shear force with  $\mu=0.3$  (Example 4.1).

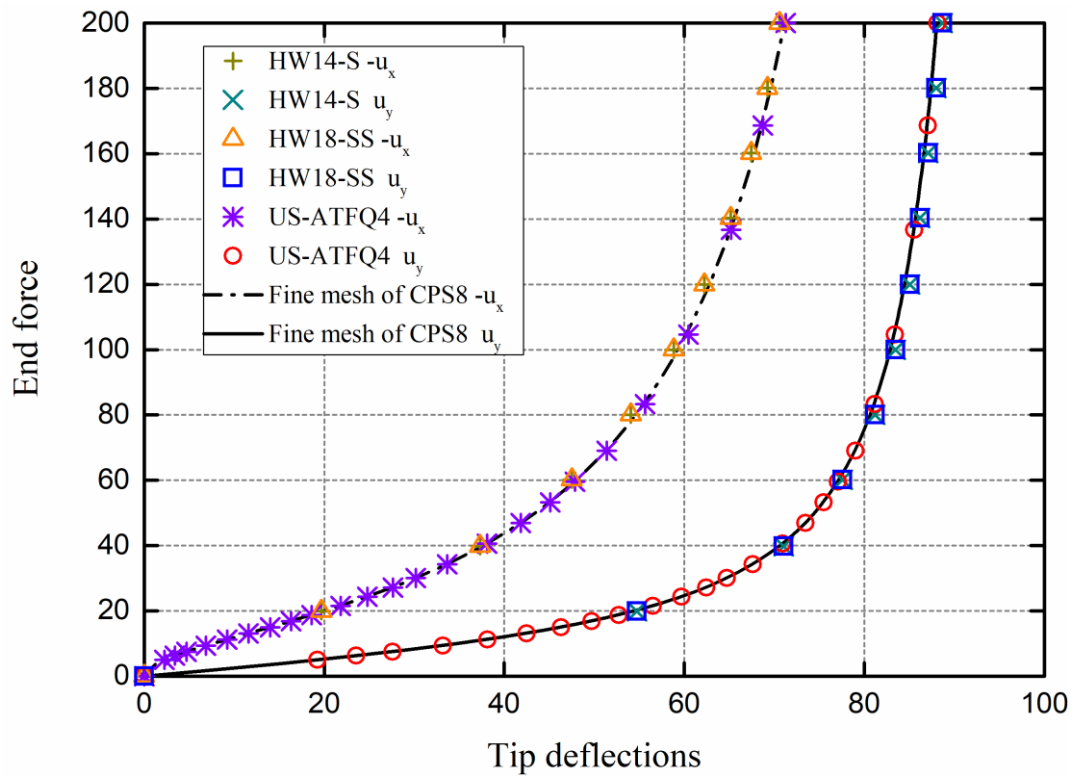


Figure 9. Load-displacement curves for a slender cantilever beam subjected to an end resultant shear force [39].

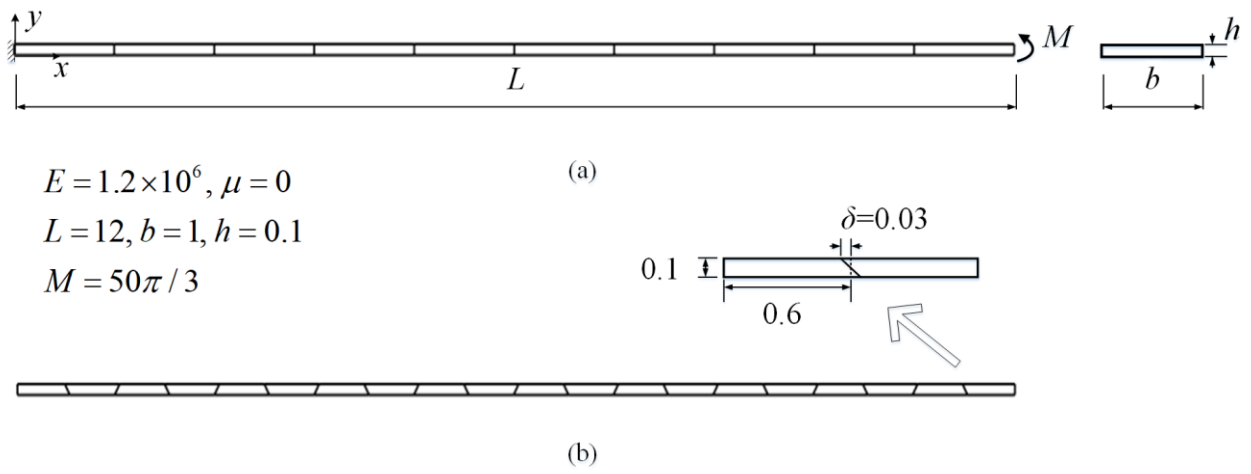
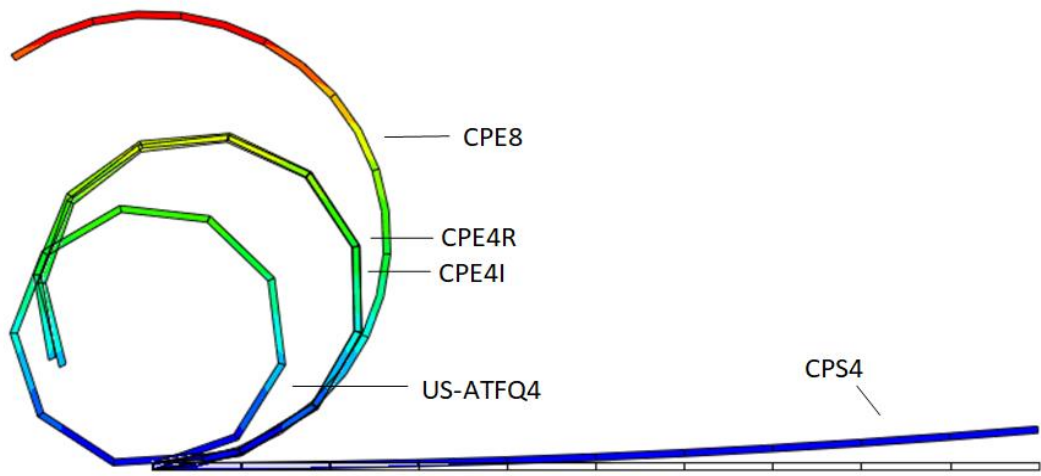
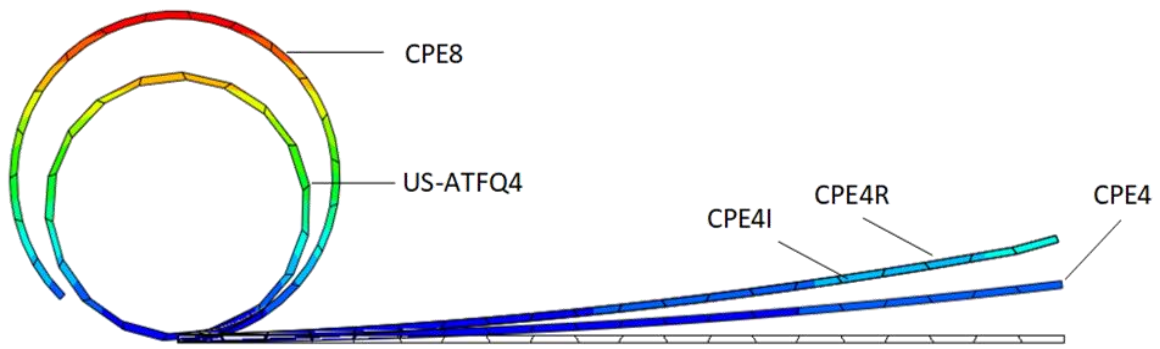


Figure 10. A slender cantilever beam subjected to end moment and two mesh cases.  
 (a) Regular mesh; (b) Distorted mesh.

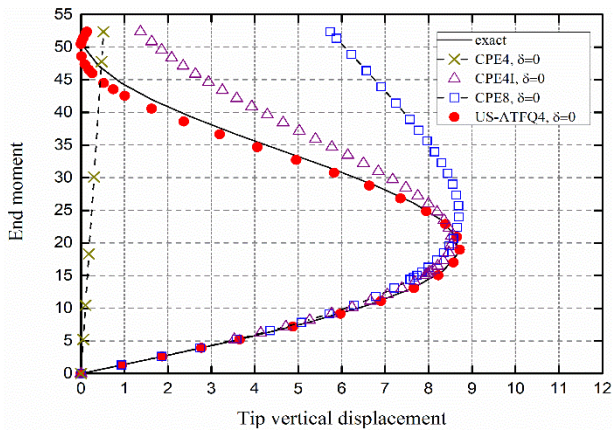


(a) Results obtained by regular mesh;

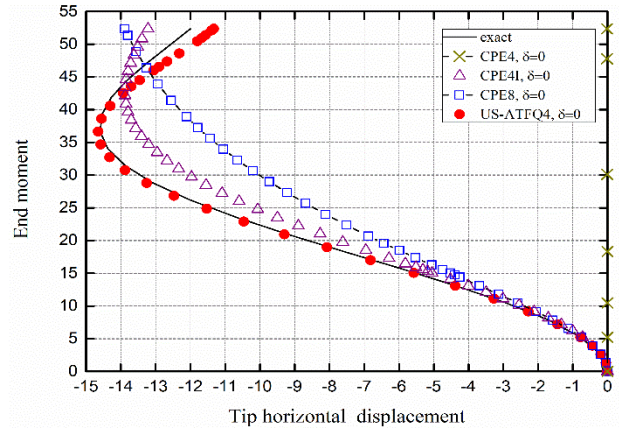


(b) Results obtained by distorted mesh.

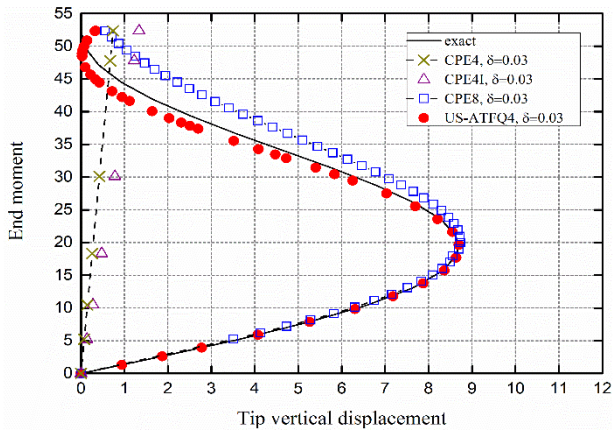
Figure 11. The deformed shapes of slender cantilever beam subjected to end resultant moment.



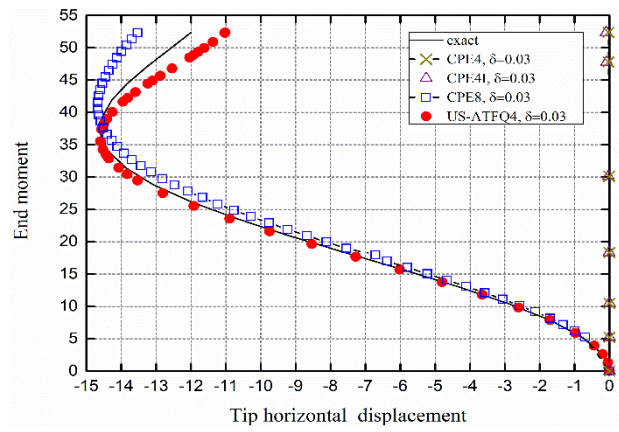
(a) End moment versus vertical displacement curves,  $1 \times 10$  regular mesh;



(b) End moment versus horizontal displacement curves,  $1 \times 10$  regular mesh;

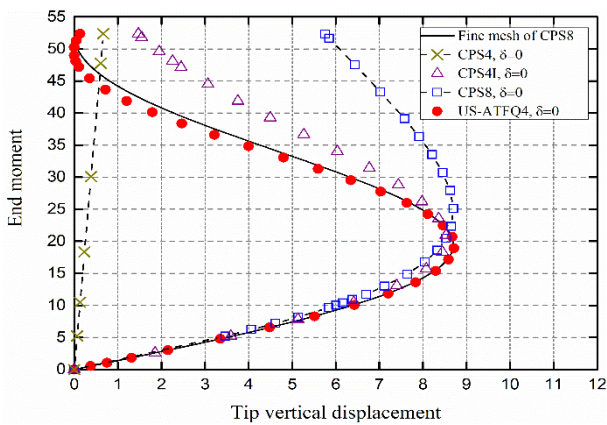


(c) End moment versus vertical displacement curves,  $1 \times 20$  distorted mesh;

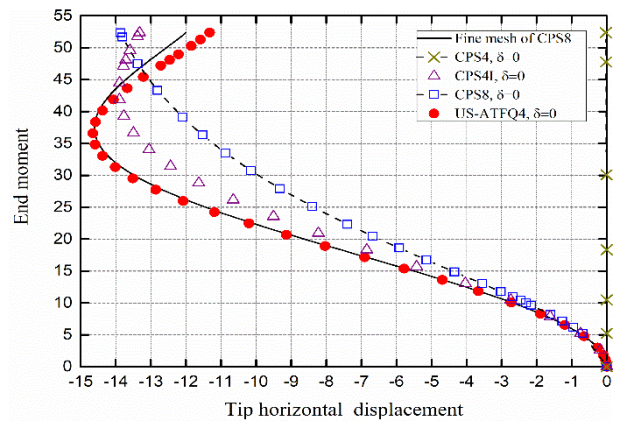


(d) End moment versus horizontal displacement curves,  $1 \times 20$  distorted mesh.

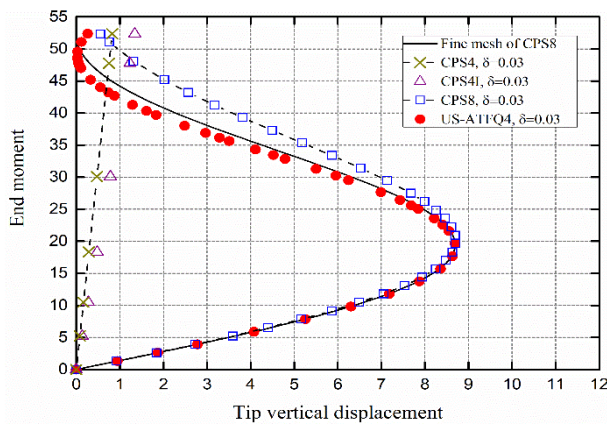
Figure 12. Load-displacement curves for a slender cantilever beam subjected to an end resultant moment with  $\mu=0$  (Example 4.2).



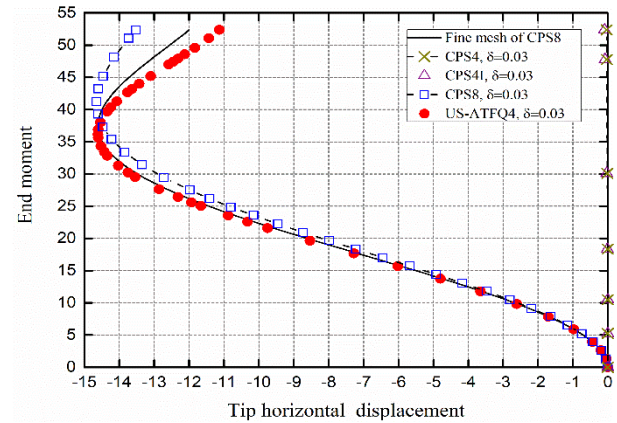
(a) End moment versus vertical displacement curves,  $1 \times 10$  regular mesh;



(b) End moment versus horizontal displacement curves,  $1 \times 10$  regular mesh;



(c) End moment versus vertical displacement curves,  $1 \times 20$  distorted mesh;



(d) End moment versus horizontal displacement curves,  $1 \times 20$  distorted mesh.

Figure 13. Load-displacement curves for a slender cantilever beam subjected to an end resultant moment with  $\mu=0.3$  (Example 4.2).

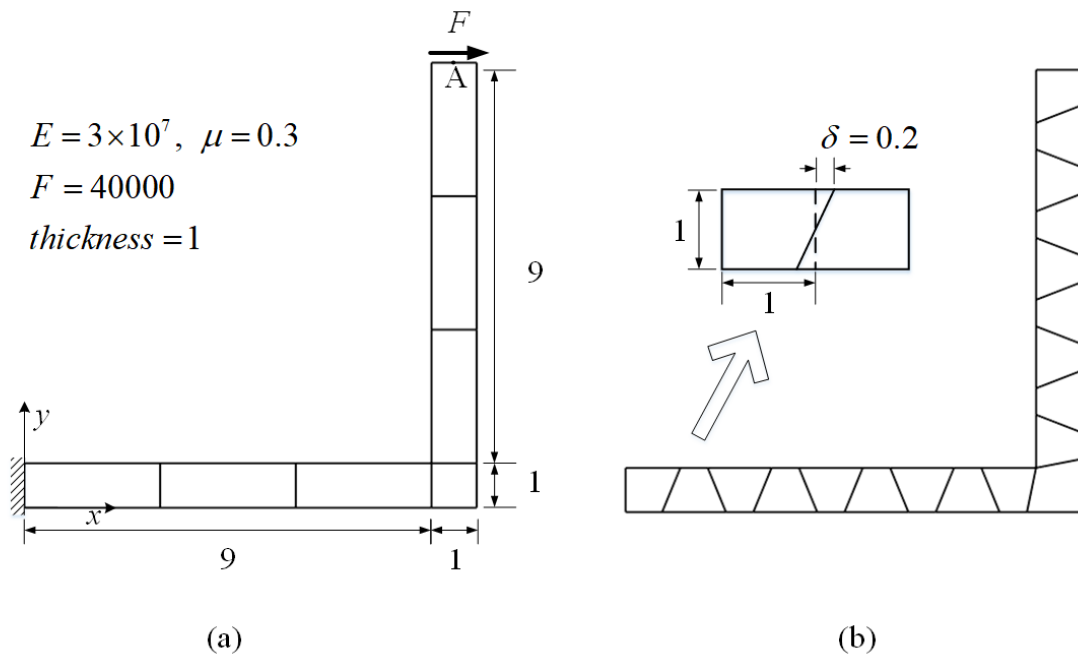
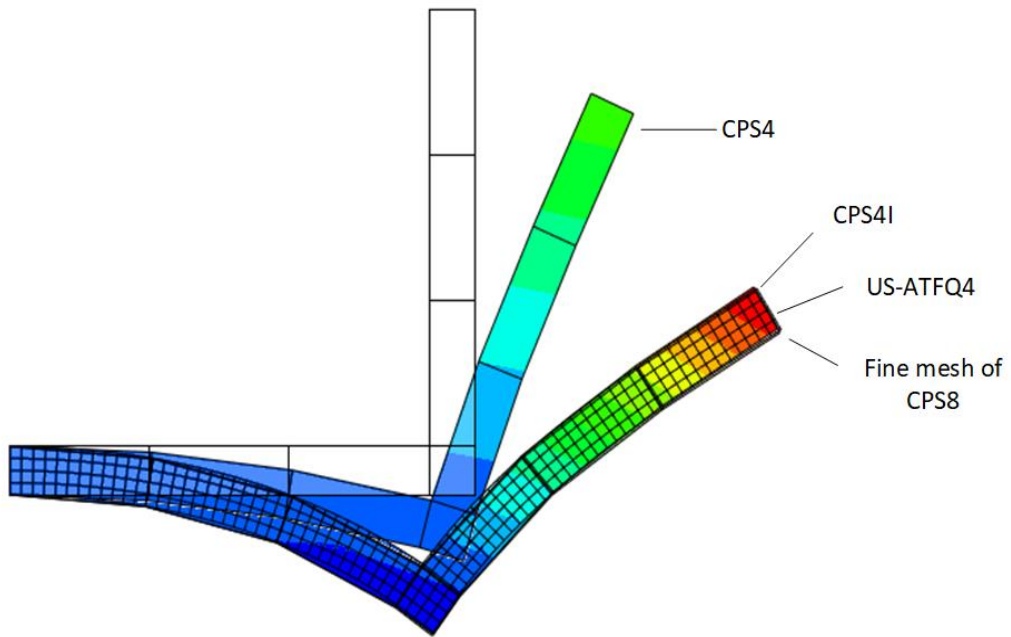
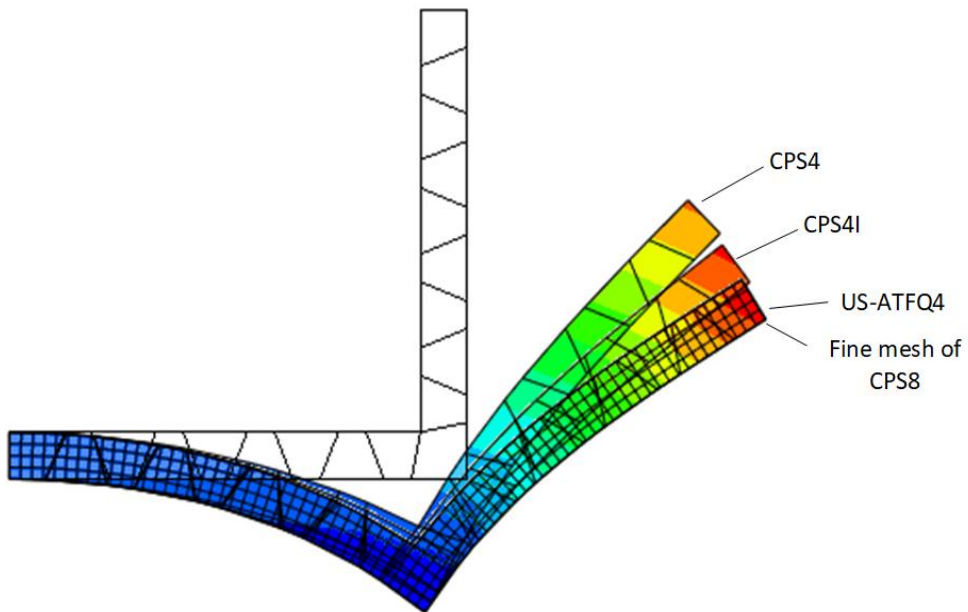


Figure 14. An angle frame structure and two mesh cases.  
 (a) Regular mesh with 7 rectangular elements; (b) Distorted mesh with 19 elements.

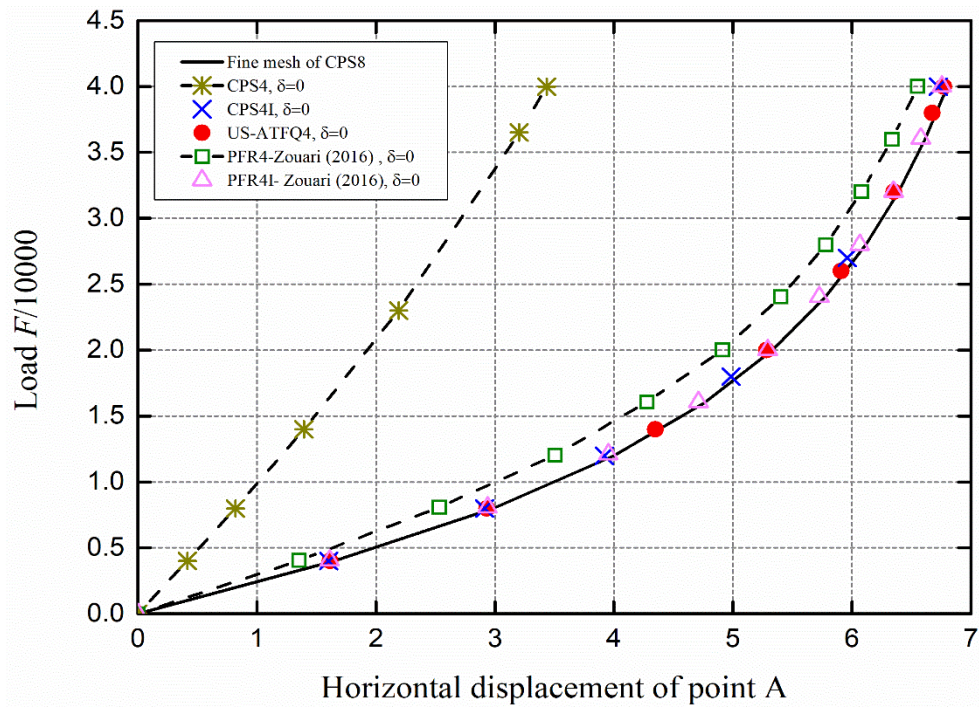


(a) Results obtained by regular mesh with 7 rectangular elements;

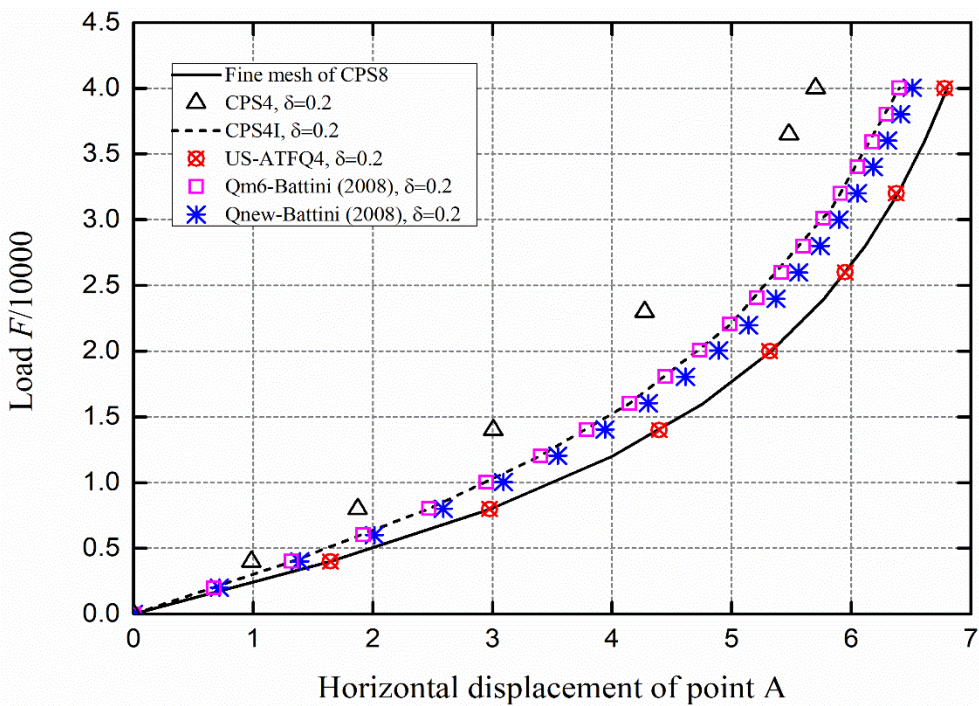


(b) Results obtained by mesh with 19 distorted elements.

Figure 15. The deformed shapes of the angle frame structure.



(a) 7 regular rectangle elements;



(b) 19 distorted elements.

Figure 16. Load versus horizontal displacement curves for the angle frame problem (Example 4.3).

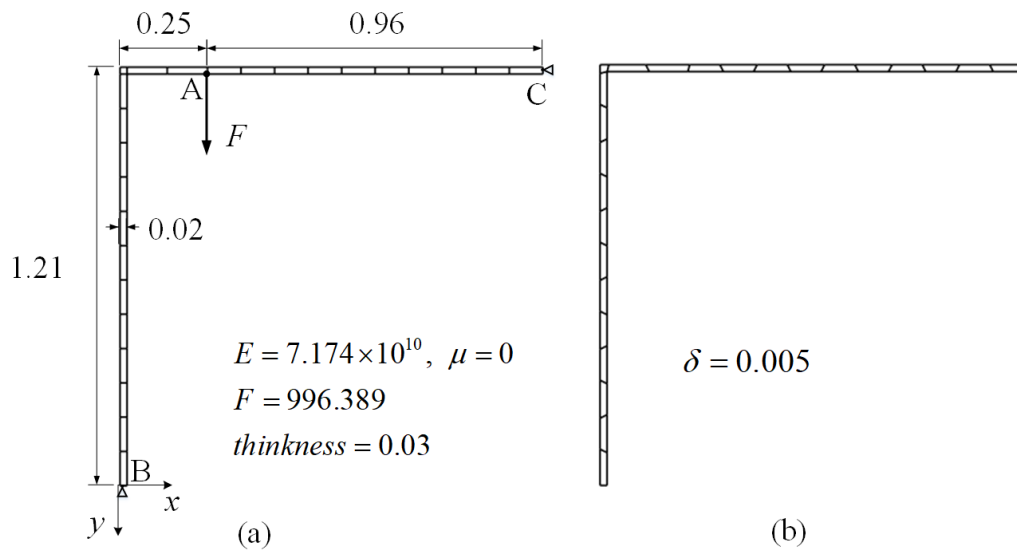


Figure 17. A Lee's frame structure and two mesh divisions.

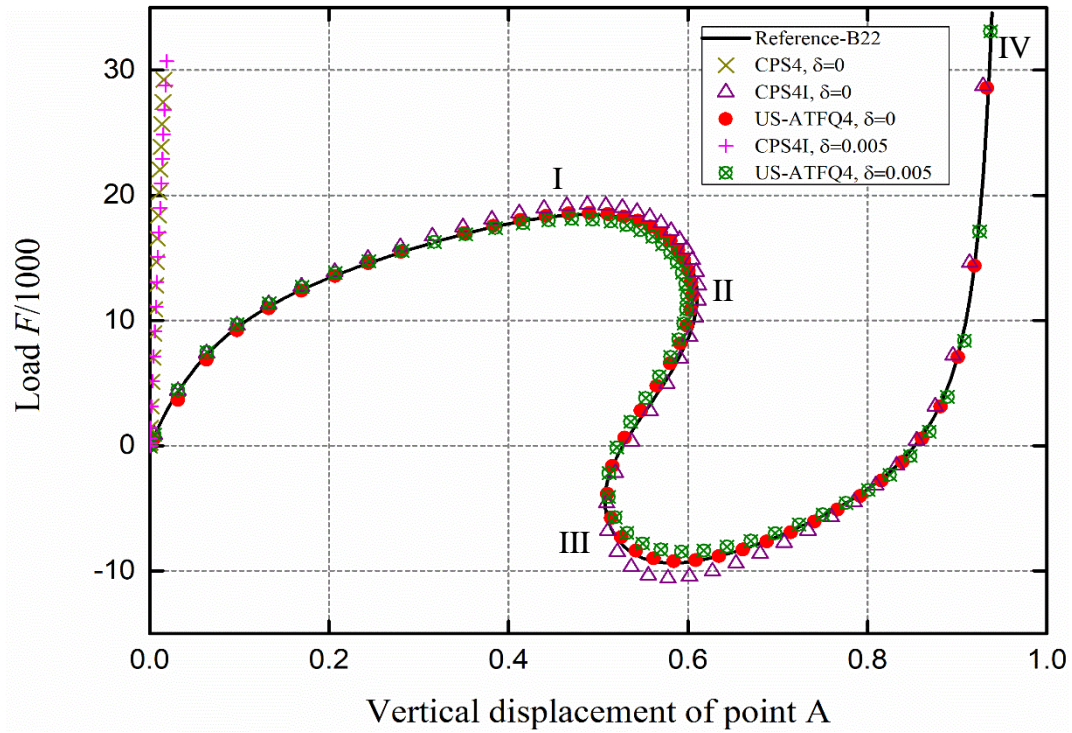


Figure 18. Load versus vertical displacement curves for the Lee's frame buckling

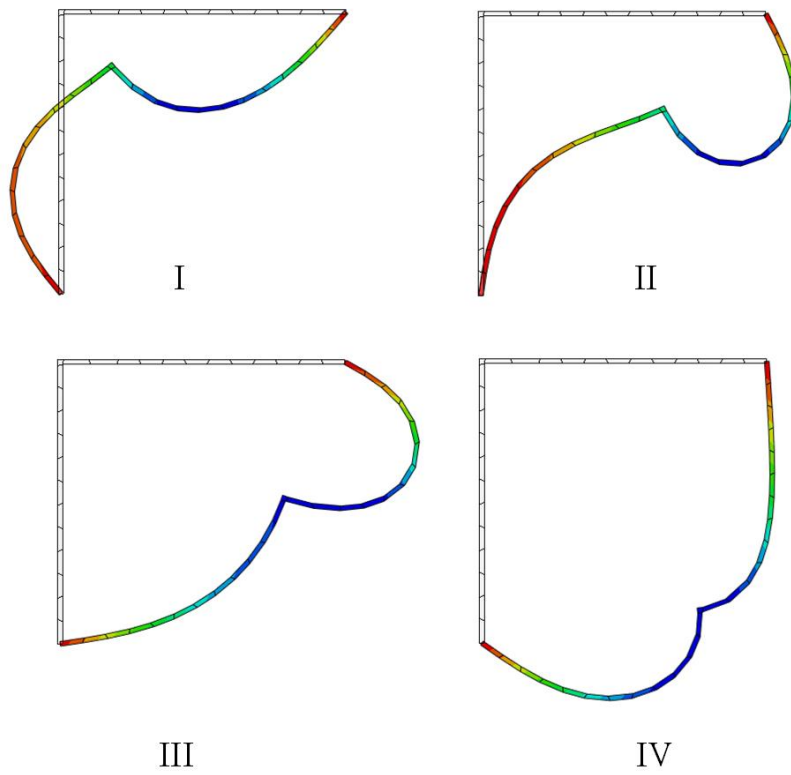


Figure 19. Four deformed states (state I, II, III and IV are given in Figure 18) of the Lee's frame structure obtained by twenty-five distorted US-ATFQ4 elements.

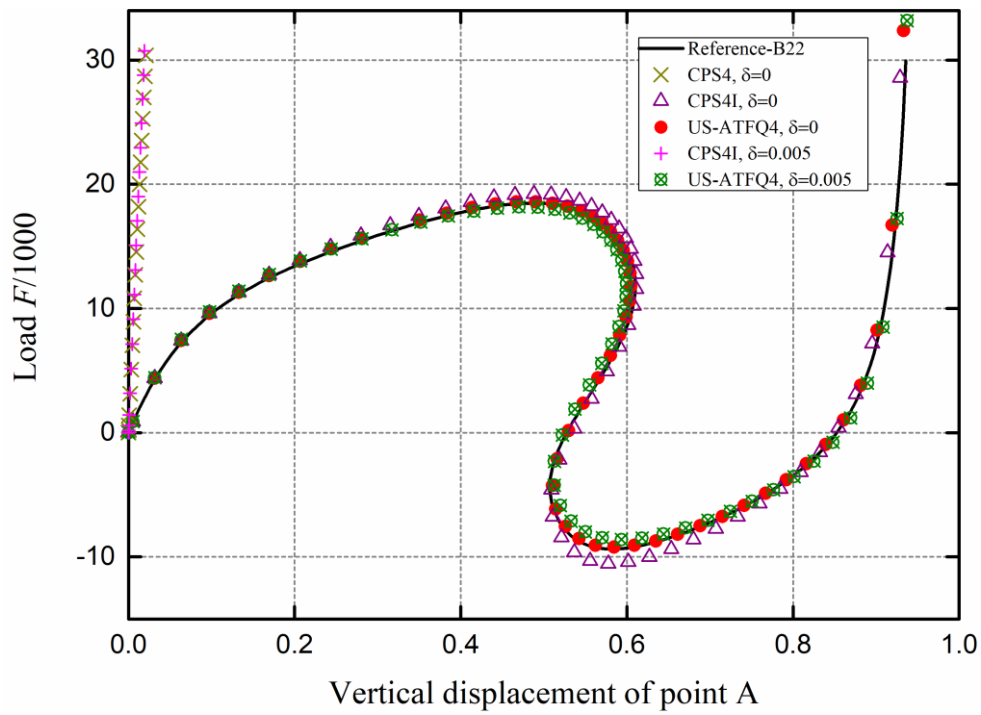


Figure 20. Load versus vertical displacement curves for the Lee's frame buckling problem with  $\mu=0.3$  (Example 4.4).

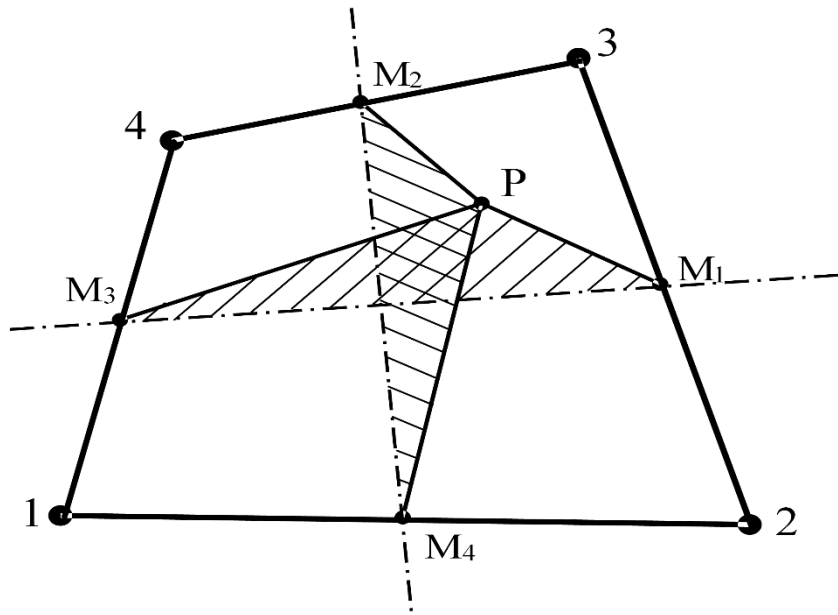


Figure A. Definition of the quadrilateral area coordinates  $S$  and  $T$  of QACM-II [24]